Journal of Inorganic Biochemistry 272 (2025) 113013

Contents lists available at ScienceDirect

Journal of Inorganic Biochemistry

journal homepage: www.elsevier.com/locate/jinorgbio

Synthesis and anticancer evaluation of tri-*n*-butyltin complexes featuring azomethine- and diazenyl-functionalized benzoates with peripheral fluorine against MDA-MB-231 breast cancer cells

Tushar S. Basu Baul [a,*], Amon Das [a], Avishek Khatiwara [a], Vivek Kumar Sharma [b], Andrew Duthie [c], Biplob Koch [b,*], Sean Parkin [d,*]

[a] Centre for Advanced Studies in Chemistry, North-Eastern Hill University, NEHU Permanent Campus, Umshing, Shillong 793 022, India
[b] Genotoxicology and Cancer Biology Laboratory, Department of Zoology, Institute of Science, Banaras Hindu University, Varanasi 221005, India
[c] School of Life & Environmental Science, Deakin University, Pigdons Road, Waurn Ponds, Victoria 3216, Australia
[d] Department of Chemistry, University of Kentucky, 506 Library Drive, 146 Chemistry-Physics Building, Lexington, KY 40506-0055, USA

ARTICLE INFO

Keywords:
Tri-n-butyltins
Hydroxyl-benzoate ligand
Fluoro derivatives
Spectroscopy
Crystal structure
Cytotoxicity

ABSTRACT

Five complexes, [*n*-$Bu_3Sn(HL^{H})$] (**1**), [*n*-$Bu_3Sn(HL^{4\text{-}F})$] (**2**), [*n*-$Bu_3Sn(HL^{2\text{-}CF3})$] (**3**), [*n*-$Bu_3Sn(HL^{3\text{-}CF3})$] (**4**) and [*n*-$Bu_3Sn(HL^{4\text{-}CF3})$] (**5**), were synthesized by reacting the corresponding azomethine- and diazenyl-functionalized hydroxy-benzoic acid pro-ligands (H'HL^{H}, H'$HL^{4\text{-}F}$, H'$HL^{2\text{-}CF3}$, H'$HL^{3\text{-}CF3}$ and H'$HL^{4\text{-}CF3}$) with (*n*-$Bu_3Sn)_2O$. Compounds **1**–**5** were thoroughly characterized by FT-IR and NMR (^{1}H, ^{13}C, and ^{119}Sn) spectroscopy. Additionally, the molecular and crystal structures of compounds **2**, **4** and **5**, along with one of their pro-ligands (H'$HL^{3\text{-}CF3}$), were determined by single-crystal X-ray diffraction analysis. The tri-*n*-butyltin(IV) complexes (**2**, **4**, and **5**) form mono-periodic chains in which the *n*-Bu_3Sn groups are linked to the oxygen atoms of the benzoate ligand through one short and one long Sn-O bond. This arrangement results in a pentacoordinated tin center, exhibiting slightly distorted *trans*-Bu_3SnO_2 trigonal-bipyramidal geometries, as indicated by their τ_5 parameters. The hydroxy H atom forms an intramolecular O–H···N hydrogen bond with the imine N-atom, as observed in the crystal structure of H'$HL^{3\text{-}CF3}$. The ^{119}Sn NMR spectra of compounds **1**–**5** showed a resonance at around +110 ppm, consistent with a tetrahedral geometry in solution. This suggests that the polymeric structures of complexes **2**, **4**, and **5** observed in the solid state dissociate upon dissolution. The *in vitro* cytotoxicity of the tri-*n*-butyl compounds **1**–**5** was assessed against MDA-MB-231 breast cancer cells. Compounds **1**–**5** showed potent cytotoxicity against MDA-MB-231 cells (IC_{50}: 0.90–2.18 μM), with the fluorinated complex [*n*-$Bu_3Sn(HL^{4\text{-}F})$] (**2**) being the most active (IC_{50} = 0.90 ± 0.05 μM). The proposed mechanism of action is discussed in light of findings from various biological assays.

1. Introduction

Recently, there has been a significant rise in interest in organotin compounds [1–4]. These compounds have long been recognized for their broad range of biological properties, including anticancer [5–21], antioxidant [11,12,20,22], antituberculosis [23,24], antileishmanial [11–13], antimicrobial [12,13,25–26], antifungal [11,27], and antimalarial [28–30] effects, among others. Beyond their well-established function as trans esterification catalysts [31], recent research has revealed additional applications in catalysis, supramolecular chemistry, and materials science. These include their use as catalysts for C - C coupling [32], activators for CO_2 [33], luminescent compounds responsive to light or electrochemical excitation [34], materials for nonlinear optics (NLO) [35], and in solar cell manufacturing [36]. Moreover, organotin compounds have been explored as molecular rotors [37], receptors for anions [38], agents for ditopic complexation [39], and even for sensing dihydrogen sulfide [39].

In recent years, organotin(IV) Schiff base carboxylates derived from amino acids with an azomethine group have gained attention due to their potential cytotoxicity, though they showed low stability [40,41]. To improve this, new organotin(IV) carboxylates with diazenyl groups were developed, enhancing both stability and cytotoxicity [42–44].

* Corresponding authors.
E-mail addresses: basubaul@nehu.ac.in, basubaulchem@gmail.com (T.S. Basu Baul).

https://doi.org/10.1016/j.jinorgbio.2025.113013
Received 29 April 2025; Received in revised form 19 July 2025; Accepted 20 July 2025
Available online 24 July 2025

Subsequently, both azomethine and diazenyl functionalities were integrated into hydroxy-benzoic acid systems, and their complexation chemistry with various triorganotins was investigated [45–53], as illustrated in Scheme 1.

In Scheme 1, structure **I** is a mononuclear Sn-complex with distorted tetrahedral coordination [45], while analogue **II** has a five-coordinate *cis*-R_3SnO_2 geometry [46]. Complex **III** shows a *trans*-R_3SnO_2 trigonal bipyramidal structure [47], as seen in the centrosymmetric dimers of **IV**. Complexes **V** and **VI** form polymeric *trans*-R_3SnO_2 arrangements [46,48,50–53], and **VII** forms a mono-periodic polymeric chain with dinuclear macrocyclic rings via bidentate carboxylate and phenoxide groups.

Triorganotin compounds and their metal complexes are gaining interest in toxicology and oncology for their therapeutic potential [6]. In non-platinum chemotherapy, tri- and di-organotin carboxylates/benzoates have shown strong anticancer activity, often outperforming conventional treatments [54–56]. They offer advantages such as better accessibility, lower toxicity, and higher effectiveness at lower doses than cisplatin, making them promising candidates for next-generation cancer therapies [6,7,57,58]. The biological effectiveness depends on the R group and ligand (L), following the order: $R_3SnL > R_2SnL_2 > RSnL_3 > R_4Sn$ (R = alkyl or aryl, L = mono-anionic ligand) [1,7].

Fluorine significantly enhances drug properties such as metabolic stability, membrane permeability, and protein binding affinity, boosting pharmaceutical effectiveness [59,60]. In 2024, several FDA-approved fluorinated drugs, especially in oncology and infectious diseases, reflect the growing trend of incorporating aliphatic fluorine, trifluoromethyl, and difluoromethyl groups [61,62]. While metallodrugs show promise, challenges like poor solubility and low bioavailability persist. Fluorinated ligands can help overcome these issues by improving physicochemical and biological properties [63]. Recently, we investigated the impact of organotin(IV) complexes with fluorinated ligands on the antiproliferative activity against DU-145 (prostate) [64], MCF-7 (breast), and HeLa (cervical) [65] cancer cells.

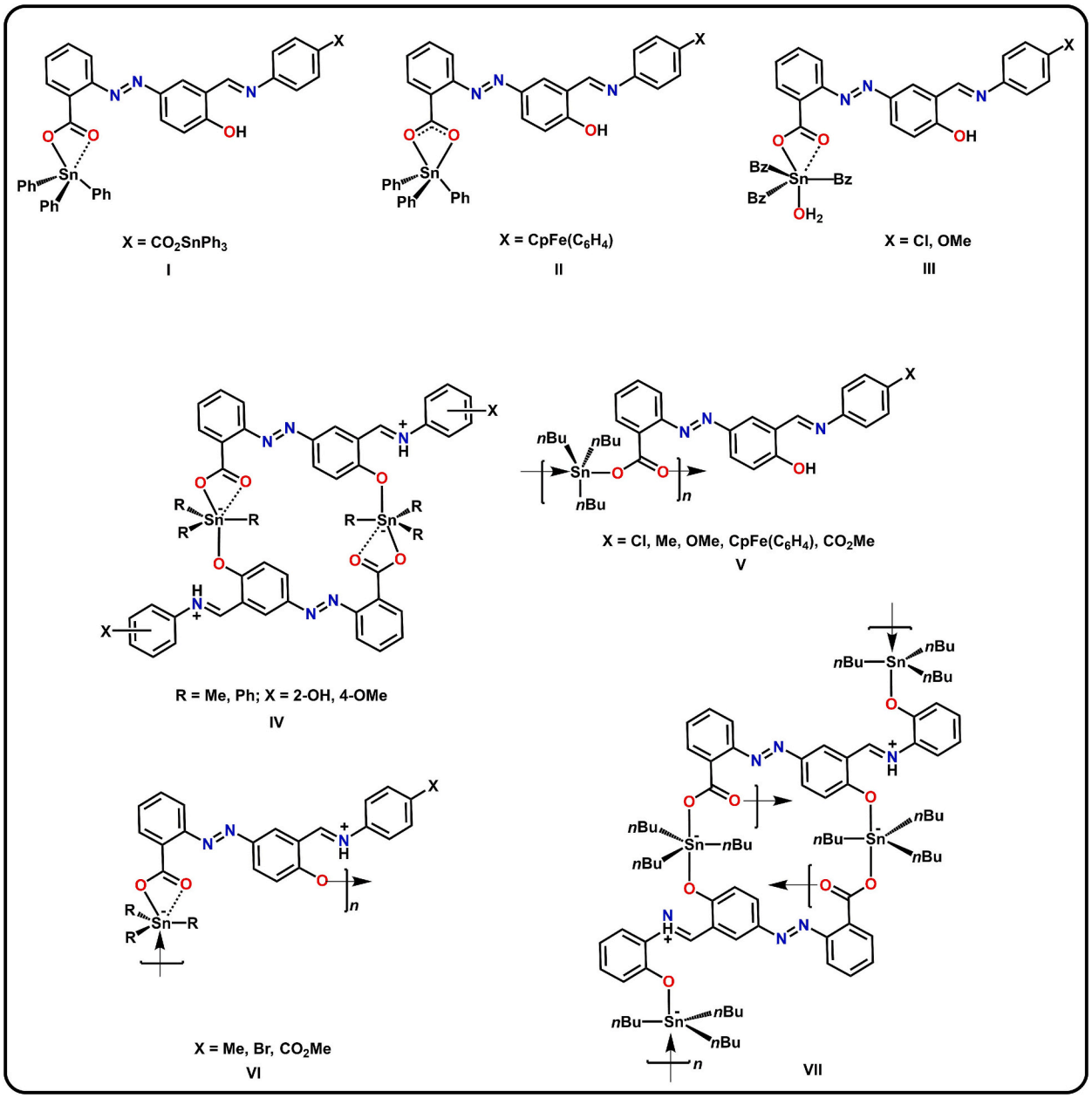

Scheme 1. Schematic representation of the coordination behavior of Schiff bases, featuring azomethine and diazenyl functionalities, toward triorganotin (IV) moieties.

In the course of this study, we have synthesized a series of novel tri-*n*-butyltin compounds incorporating fluorine-substituted Schiff bases (e.g., -F or -CF_3) that feature azomethine/diazenyl groups. The compounds include: [*n*-$Bu_3Sn(HL^{4\text{-}F})$] (**2**), [*n*-$Bu_3Sn(HL^{2\text{-}CF3})$] (**3**), [*n*-$Bu_3Sn(HL^{3\text{-}CF3})$] (**4**), and [*n*-$Bu_3Sn(HL^{4\text{-}CF3})$] (**5**), with [*n*-$Bu_3Sn(HL^{H})$] (**1**), as a fluorine-free control. Structures of the compounds were thoroughly characterized by NMR spectroscopy, and diffraction (for **2**, **4**, **5**, and $H'HL^{3\text{-}CF3}$). The in vitro antiproliferative activity of compounds **1**–**5** was evaluated on MDA-MB-231 (breast cancer) and HEK-293 (normal human embryonic kidney) cells using MTT (3-(4,5-dimethylthiazol-2-yl)-2,5-diphenyltetrazolium bromide) assays. Mechanistic studies for compound **2** was examined through AO/EB (acridine orange/ethidium bromide) staining; ROS (reactive oxygen species) levels with DCFH-DA (dichlorodihydro-fluorescein diacetate) assays, along with assessments of mitochondrial dynamics and distribution. Flow cytometry was used to investigate the effect of compound **2** on cell cycle progression and distribution among different phases (G0/G1, S, and G2/M

2. Experimental

2.1. Materials and physical measurements

Regents such as 4-fluoroaniline (Spectrochem), 2-(trifluoromethyl) aniline, 3-(trifluoromethyl)aniline (Sigma-Aldrich), 4-(trifluoromethyl) aniline (Sigma-Aldrich), anthranilic acid (Sigma-Aldrich), salicylic acid (Merck), and tri-*n*-butyltin chloride, bis(tri-*n*-butyltin)oxide (Lancaster) were used as received without further purification, while aniline (Rasayan) was distilled before use. The solvents employed in the reactions were of analytical reagent grade and were dried according to standard procedures. Toluene and hexane were distilled over benzophenone/sodium, and methanol was distilled over activated magnesium.

The MDA-MB-231 cell line, a model for triple-negative breast cancer, was acquired from the National Centre for Cell Science (NCCS) in Pune, India. For the biological experiments, 12-well and 6-well cell culture plates, Dulbecco's Modified Eagle Medium (DMEM), fetal bovine serum (FBS), penicillin-streptomycin solution, and trypsin-EDTA were sourced from Cell Clone. Additionally, 96-well plates and T-25 cell culture flasks were obtained from Eppendorf. Reagents such as MTT (Himedia), dimethyl sulfoxide (DMSO; Merck), 2′,7′-dichlorodihydrofluorescein diacetate (DCFH-DA; Sigma-Aldrich), propidium iodide (PI; SRL), acridine orange (AO; Real Gene), ethidium bromide (EB; Loba Chemie), and cisplatin (*cis*-diamminedichloroplatinum(II); CDDP) along with other analytical-grade chemicals were utilized. Melting points were determined using a Büchi M-560 melting point apparatus and are uncorrected. The Fourier Transform infrared (FT-IR) spectra of the pro-ligands ($H'HL^{H}$, $H'HL^{4\text{-}F}$, $H'HL^{2\text{-}CF3}$, $H'HL^{3\text{-}CF3}$, $H'HL^{4\text{-}CF3}$) and tri-*n*-butyltin compounds **1**–**5** were recorded in the range of 400 to 4000 cm^{-1} using a PerkinElmer Spectrum Two spectrometer equipped with UATR accessories, with a resolution of 0.5 cm^{-1}. Solution ^{1}H (400.13 MHz), ^{13}C (100.62 MHz), ^{19}F (376.3 MHz) and ^{119}Sn (149.15 MHz) nuclear magnetic resonance (NMR) spectra were recorded in $CDCl_3$ and/or DMSO-d_6 as noted, using JEOL Zeta ECZ 400R and Bruker Avance II 400, AMX 400 or Avance IV 400 spectrometers. ^{1}H, ^{13}C, ^{19}F and ^{119}Sn chemical shifts were referenced to Me_4Si (δ 0.00 ppm), $CDCl_3$ (δ 77.00 ppm), $CFCl_3$ (δ 0.00 ppm) and Me_4Sn (δ 0.00 ppm), respectively. Absorption measurements of pro-ligands and tri-*n*-butyltin compounds **1**–**5** were conducted using an Agilent Technologies Cary 60 spectrophotometer at ambient temperature in freshly prepared DMSO solution (spectroscopy grade, Merck). High-resolution mass spectra (HRMS) of **1**–**5** were acquired on a Waters Xevo G2-XS QTOF mass spectrometer employing electrospray ionization. For the biological studies, a microplate reader (Biorad) and inverted fluorescence microscopes (Evos FL, Life technologies, AMF4300) were utilized. Crystallographic details are given below.

2.2. Synthesis of the pre-ligand 2-[(E)-2-(3-formyl-4-hydroxyphenyl)-1-diazenyl]benzoic acid (H'HL)

The pre-ligand, H'HL, was synthesized via a diazo-coupling reaction between anthranilic acid and salicylaldehyde in an alkaline solution under cold conditions, following the method outlined in a previous report [66]. The crude product was recrystallized from toluene, yielding a yellow microcrystalline product. The melting point (M.p.: 177–178 °C) and spectroscopic data were then re-examined to assess the purity before its use.

2.3. Synthesis of the pro-ligands

2.3.1. Synthesis of 2-((E)-(4-hydroxy-3-((E)-(phenylimino)methyl) phenyl)diazenyl)benzoic acid ($H'HL^{H}$)

The pro-ligand, $H'HL^{H}$, was synthesized by reacting equimolar amounts of an ethanolic solution (2 mL) of aniline (0.34 g, 3.70 mmol) with hot toluene (40 mL) containing 2-[(*E*)-2-(3-formyl-4-hydroxyphenyl)-1-diazenyl]benzoic acid (H'HL) (1.0 g, 3.70 mmol). The reaction mixture was heated under reflux for 4 h using a Dean-Stark apparatus with a water-cooled condenser. Afterward, the reaction mixture was concentrated to half its initial volume using a rotary evaporator and cooled to room temperature, whereupon a yellow solid precipitated. The precipitate was then washed with hexane (3 × 5 mL) and dried under vacuum. The yellow mass was dissolved in saturated hot aqueous solution of sodium bicarbonate and filtered while still hot. The filtrate was then precipitated by the slow addition of dilute acetic acid, with continuous stirring, resulting in the formation of a yellow precipitate. This precipitate was filtered, washed with water until the pH reached neutral, and then dried. The crude product was boiled with hexane (3 × 5 mL), filtered, dried, and recrystallized from toluene, yielding a brick-red solid. Yield: 1.1 g, (86 %). M.p.: 204–205 °C. FT-IR (ATR mode; ν in cm^{-1}): 1728 (w) $\nu(OCO)_{asy}$, 1637 (w), 1612 (w), 1591 (s), 1523 (w), 1496 (m), 1463 (w), 1395 (m), 1274 (m), 1245 (w), 1129 (m), 1107 (m), 1084 (m), 1014 (m), 880 (m), 839 (m), 820 (s), 756 (vs), 746 (vs), 682 (vs), 651 (s). ^{1}H NMR ($CDCl_3$): $\delta = 14.46$ (s, 1H, OH), 8.72 (s, 1H, C(*H*)N), 8.37 (d,$^{3}J(^{1}H\text{-}^{1}H) = 7.5$ Hz, 1H, ArH), 7.97 (m, 2H, ArH), 7.89 (d,$^{3}J(^{1}H\text{-}^{1}H) = 9.0$ Hz, 1H, ArH), 7.61 (m, 2H, ArH), 7.42 (m, 2H, ArH), 7.30 (m, 3H, ArH), 7.14 (d,$^{3}J(^{1}H\text{-}^{1}H) = 9.0$ Hz, 1H, ArH) ppm. ^{13}C NMR (1:1; $CDCl_3$/DMSO-d_6): δ = 164.68 (COO), 161.02 (C(*H*)N) and COH, 149.67, 145.86, 143.89, 131.23, 129.61, 129.32, 128.86, 128.60, 128.31, 126.62, 126.33, 120.28, 117.90, 117.68, 116.19 (ArC) ppm. Electronic absorption data (DMSO, λ_{max}[nm]; $\varepsilon(M^{-1}\ cm^{-1})$): 331, 7470.

2.3.2. Synthesis of 2-((E)-(3-((E)-((4-fluorophenyl)imino)methyl)-4-hydroxyphenyl)diazenyl)benzoic acid ($H'HL^{4\text{-}F}$)

An analogous procedure to that used for the preparation of $H'HL^{H}$ was followed, employing 4-fluoroaniline (0.41 g, 3.70 mmol) and 2-[(*E*)-2-(3-formyl-4-hydroxyphenyl)-1-diazenyl]benzoic acid (H'HL) (1.0 g, 3.70 mmol). The resulting yellow precipitated was isolated using the work up procedure described for $H'HL^{H}$ and recrystallized from toluene, yielding a brick-red solid. Yield: 1.21 g, (90 %). M.p.: 221–222 °C. FT-IR (ATR mode; ν in cm^{-1}): 1729 (s) $\nu(OCO)_{asy}$, 1696 (w), 1618 (vs), 1595 (s), 1579 (w), 1505 (vs), 1496 (vs), 1476 (s), 1356 (w), 1296 (w), 1228 (s), 1183 (m), 1148 (m), 1101 (m), 1030 (w), 886 (w), 830 (vs), 797 (m), 760 (s), 742 (m), 686 (s), 663 (w), 626 (w). ^{1}H NMR ($CDCl_3$): $\delta = 8.67$ (s, 1H, C(*H*)N), 8.36 (d,$^{3}J(^{1}H\text{-}^{1}H) = 7.5$ Hz, 1H, ArH), 7.95 (m, 2H, ArH), 7.88 (d,$^{3}J(^{1}H\text{-}^{1}H) = 9.0$ Hz, 1H, ArH), 7.60 (m, 2H, ArH), 7.28 (m, 2H, ArH), 7.11 (m, 3H, ArH) ppm. ^{13}C NMR (1:1; $CDCl_3$/DMSO-d_6): δ = 168.47 (COO), 163.80 (COH), 162.54 (C(*H*)N), 161.24 (d,$^{1}J(^{13}C\text{-}^{19}F)$ = 245 Hz), 150.86, 144.96, 143.94 (d,$^{4}J(^{13}C\text{-}^{19}F) = 3$ Hz), 131.67, 130.15, 129.27, 128.82, 126.68, 123.48 (d,$^{3}J(^{13}C\text{-}^{19}F) = 8$ Hz), 119.32, 118.33, 118.09, 116.30 (d,$^{2}J(^{13}C\text{-}^{19}F) = 23$ Hz) (ArC) ppm. ^{19}F NMR ($CDCl_3$); δ = − 114.9 ppm. Electronic absorption data (DMSO, λ_{max}[nm]; $\varepsilon(M^{-1}\ cm^{-1})$): 336, 5010.

2.3.3. Synthesis of 2-((E)-(4-hydroxy-3-((E)-((2-(trifluoromethyl)phenyl) imino)methyl)phenyl)diazenyl)benzoic acid (H'HL$^{2\text{-}CF3}$)

An analogous procedure to that used for the preparation of H'HL^{H} was followed, employing 2-(trifluoromethyl)aniline (0.60 g, 3.70 mmol) and 2-[(*E*)-2-(3-formyl-4-hydroxyphenyl)-1-diazenyl]benzoic acid (H'HL) (1.0 g, 3.70 mmol). The resulting brick-red crystalline material was isolated using the work up procedure described for H'HL^{H} and recrystallized from toluene, yielding a brick-red solid. Yield: 1.32 g, (86 %). M.p.: 188–189 °C. FT-IR (ATR mode; ν in cm^{-1}): 1727 (m) ν(OCO)$_{asy}$, 1674 (w), 1614 (s), 1573 (s), 1470 (m), 1451 (m), 1416 (w), 1354 (w), 1313 (s), 1286 (m), 1268 (s), 1239 (w), 1150 (s), 1119 (s), 1105 (vs), 1051 (m), 1035 (m), 973 (w), 896 (w), 863 (m), 822 (m), 760 (vs), 753 (vs), 738 (m), 686 (s), 643 (w), 628 (w). ^{1}H NMR ($CDCl_3$): δ = 13.48 (s, 1H, OH), 8.68 (s, 1H, C(*H*)N), 8.34 (d,^{3}J(^{1}H-^{1}H) = 7.5 Hz, 1H, ArH), 7.92 (m, 3H, ArH), 7.69 (d,^{3}J(^{1}H-^{1}H) = 7.7 Hz, 1H, ArH), 7.60 (m, 3H, ArH), 7.37 (t,^{3}J(^{1}H-^{1}H) = 9.0 Hz, 1H, ArH), 7.27 (d,^{3}J(^{1}H-^{1}H) = 7.7 Hz, 1H, ArH), 7.15 (d,^{3}J(^{1}H-^{1}H) = 9.0 Hz, 1H, ArH) ppm. ^{13}C NMR (1:1; $CDCl_3$/DMSO-d_6): δ = 166.91 (COO), 164.84 (COH), 163.03 (C(*H*)N), 149.78, 145.23, 144.35, 133.11, 132.70, 131.38, 130.77, 129.68, 127.68, 127.25, 127.79, 126.26 (q,^{3}J(^{13}C-^{19}F) = 8 Hz), 123.72 (q,^{2}J (^{13}C-^{19}F) = 30 Hz), 123.37 (q,^{1}J(^{13}C-^{19}F) = 274 Hz, CF_3), 119.06, 118.63, 118.54, 116.15 (ArC) ppm. ^{19}F NMR ($CDCl_3$); δ = − 60.4 ppm. Electronic absorption data (DMSO, λ_{max}[nm]; ε(M^{-1} cm^{-1}): 334, 3230.

2.3.4. Synthesis of 2-((E)-(4-hydroxy-3-((E)-((3-(trifluoromethyl)phenyl) imino)methyl)phenyl)diazenyl)benzoic acid (H'HL$^{3\text{-}CF3}$)

An analogous procedure to that used for the preparation of H'HL^{H} was followed, employing 3-(trifluoromethyl)aniline (0.60 g, 3.70 mmol) and 2-[(*E*)-2-(3-formyl-4-hydroxyphenyl)-1-diazenyl]benzoic acid (H'HL) (1.0 g, 3.70 mmol). The resulting brick-red crystalline material was isolated using the work up procedure described for H'HL^{H} and recrystallized from toluene, yielding a brick-red solid. Yield: 1.20 g, (78 %). M.p.: 177–178 °C. FT-IR (ATR mode; ν in cm^{-1}): 1721 (vs) ν(OCO)$_{asy}$, 1620 (m), 1593 (m), 1564 (m), 1482 (m), 1468 (m), 1410 (m), 1364 (s), 1323 (vs), 1280 (m), 1257 (m), 1206 (w), 1177 (m), 1154 (s), 1119 (s), 1105 (vs), 1059 (m), 892 (m), 804 (s), 762 (vs), 740 (w), 682 (vs), 655 (w), 626 (w). ^{1}H NMR ($CDCl_3$): δ = 13.81 (s, 1H, OH), 8.72 (s, 1H, C(*H*)N), 8.34 (d,^{3}J(^{1}H-^{1}H) = 7.5 Hz, 1H, ArH), 7.97 (s, 1H, ArH), 7.93 (d,^{3}J(^{1}H-^{1}H) = 8.0 Hz, 1H, ArH), 7.88 (d,^{3}J(^{1}H-^{1}H) = 9.0 Hz, 1H, ArH), 7.57 (m, 5H, ArH), 7.45 (m, 1H, ArH), 7.13 (d,^{3}J(^{1}H-^{1}H) = 9.0 Hz, 1H, ArH) ppm. ^{13}C NMR ($CDCl_3$): δ = 166.19 (COO), 166.15 (COH), 162.86 (C(*H*)N), 149.38, 147.64, 144.18, 133.72, 132.94, 132.09 (q,^{2}J (^{13}C-^{19}F) = 30 Hz), 131.99, 130.25, 130.08, 127.96, 126.43, 124.48, 124.24 (q,^{3}J(^{13}C-^{19}F) = 4 Hz), 123.62 (q,^{1}J(^{13}C-^{19}F) = 273 Hz, CF_3), 119.36, 118.94, 118.29 (q,^{3}J(^{13}C-^{19}F) = 4 Hz), 115.71 (ArC) ppm. ^{19}F NMR ($CDCl_3$); δ = − 62.7 ppm. Electronic absorption data (DMSO, λ_{max}[nm]; ε(M^{-1} cm^{-1}): 332, 2645.

2.3.5. Synthesis of 2-((E)-(4-hydroxy-3-((E)-((4-(trifluoromethyl)phenyl) imino)methyl)phenyl)diazenyl)benzoic acid (H'HL$^{4\text{-}CF3}$)

An analogous procedure to that used for the preparation of H'HL^{H} was followed, employing 4-(trifluoromethyl)aniline (0.60 g, 3.70 mmol) and 2-[(*E*)-2-(3-formyl-4-hydroxyphenyl)-1-diazenyl]benzoic acid (H'HL) (1.0 g, 3.70 mmol). The resulting brick-red crystalline material was isolated using the work up procedure described for H'HL^{H} and recrystallized from toluene, yielding a brick-red solid. Yield: 1.25 g, (82 %). M.p.: 204–205 °C. FT-IR (ATR mode; ν in cm^{-1}): 1729 (vs) ν(OCO)$_{asy}$, 1624 (w), 1604 (s), 1579 (m), 1478 (m), 1321 (vs), 1278 (w), 1245 (w), 1167 (s), 1148 (w), 1107 (vs), 1065 (vs), 1012 (m), 884 (m), 837 (w), 824 (s), 764 (s), 688 (s), 610 (w). ^{1}H NMR ($CDCl_3$): δ = 13.90 (s, 1H, OH), 8.79 (s, 1H, C(*H*)N), 8.42 (d,^{3}J(^{1}H-^{1}H) = 7.5 Hz, 1H, ArH), 8.04 (s, 1H, ArH), 8.01 (d,^{3}J(^{1}H-^{1}H) = 8.0 Hz, 1H, ArH), 7.96 (d,^{3}J (^{1}H-^{1}H) = 9.0 Hz, 1H, ArH), 7.74 (d,^{3}J(^{1}H-^{1}H) = 8.0 Hz, 2H, ArH), 7.68 (m, 2H, ArH), 7.44 (d,^{3}J(^{1}H-^{1}H) = 8.0 Hz, 2H, ArH), 7.36 (toluene), 7.21 (d,^{3}J(^{1}H-^{1}H) = 9.0 Hz, 1H, ArH) ppm. ^{13}C NMR ($CDCl_3$): δ = 166.25 (COO and COH), 163.27 (C(*H*)N), 150.18, 149.47, 144.32, 133.77, 133.05, 132.10, 129.99, 129.58 (q,^{2}J(^{13}C-^{19}F) = 33 Hz), 128.26, 126.86 (q,^{3}J(^{13}C-^{19}F) = 4 Hz), 126.52, 123.88 (q,^{1}J(^{13}C-^{19}F) = 272 Hz, CF_3), 121.58, 119.46, 118.99, 115.76 (ArC) ppm. ^{19}F NMR ($CDCl_3$); δ = − 62.3 ppm. Electronic absorption data (DMSO, λ_{max}[nm]; ε(M^{-1} cm^{-1}): 337, 2130.

2.4. Synthesis of tri-n-butyltin compounds

2.4.1. Synthesis of [n-Bu$_3$Sn(HL^{H})]$_n$ (1)

Compound **1** was synthesized by reacting H'HL^{H} (0.25 g, 0.72 mmol) with (*n*-Bu$_3$Sn)$_2$O (0.216 g, 0.36 mmol) in 50 mL of anhydrous toluene, using a Dean-Stark moisture trap and a water-cooled condenser. The reaction mixture was refluxed for 6 h and then filtered while still hot. The resulting clear dark-red solution was evaporated to dryness using a rotary evaporator and then dried under vacuum. The dark-red oil was triturated with hexane (3 × 1.0 mL) in an ice-salt bath and filtered. The precipitation process was repeated three times, after which the product was dried in vacuo. Crystallization from anhydrous hexane, followed by slow evaporation at room temperature, yielded orange crystalline compound **1**. Yield: 0.25 g (57 %), M.p.: 122–123 °C. FT-IR (ATR mode; ν in cm^{-1}): 2923 (w) ν(C-H)$_{aliphatic}$, 1614 (s) ν(OCO)$_{asy}$, 1579 (s), 1546 (vs), 1486 (m), 1459 (w), 1391 (vs) ν(OCO)$_{sy}$, 1350 (m), 1282 (m), 1144 (s), 1088 (w), 954 (m), 901 (m), 872 (m), 849 (m), 830 (s), 760 (s), 738 (s), 684 (m), 663 (vs). ^{1}H NMR ($CDCl_3$): δ = 13.89 (s, 1H, OH), 8.74 (s, 1H, C(*H*)N), 8.05 (s, 1H, ArH), 8.01 (d,^{3}J(^{1}H-^{1}H) = 9.0 Hz, 1H, ArH), 7.82 (d,^{3}J(^{1}H-^{1}H) = 7.5 Hz, 1H, ArH), 7.48 (m, 5H, ArH), 7.33 (m, 3H, ArH), 7.12 (d,^{3}J(^{1}H-^{1}H) = 9.0 Hz, 1H, ArH), 1.62 (m, 6H, *n*-Bu-1), 1.32 (m, 12H, *n*-Bu-2/3), 0.87 (t, 9H, *n*-Bu-4) ppm. ^{13}C NMR ($CDCl_3$): δ = 172.62 (COO), 164.16 (COH), 161.97 (C(*H*)N), 151.82, 147.74, 145.81, 131.41, 130.83, 129.82, 129.49, 129.20, 128.79, 127.32, 121.12, 118.73, 118.03, 117.68 (ArC), 27.81 (^{2}J(^{13}C-^{119}Sn) = 20 Hz, *n*-Bu-2), 27.03 (^{3}J[^{13}C-^{119}Sn] = 64 Hz, *n*-Bu-3), 16.67 (^{1}J(^{13}C-$^{117/119}$Sn) = 339/355 Hz, *n*-Bu-1), 13.58 (*n*-Bu-4) ppm.^{119}Sn NMR ($CDCl_3$); δ = +115.9 ppm. Electronic absorption data (DMSO, λ_{max}[nm]; ε(M^{-1} cm^{-1}): 330, 1996. HRMS-ESI^{+} (*m/z*, %): found 291.1077 (33), calcd. For [Bu$_3$Sn]$^{+}$ 291.1135; found 625.2064 (55), calcd. For [(Bu$_3$Sn)$_2$CO$_2$H] $^{+}$ 625.2240.

2.4.2. Synthesis of [n-Bu$_3$Sn(HL$^{4\text{-}F}$)]$_n$ (2)

An analogous method to that used for preparing compound **1** was employed, utilizing (*n*-Bu$_3$Sn)$_2$O (0.164 g, 0.275 mmol) and H'HL$^{4\text{-}F}$ (0.20 g, 0.55 mmol). Following the workup, crystallization from anhydrous hexane and slow evaporation at room temperature resulted in the formation of orange crystals of compound **2**. Yield: 0.21 g (60 %), M.p.: 101–102 °C. FT-IR (ATR mode; ν in cm^{-1}): 2925 (w) ν(C-H)$_{aliphatic}$, 1618 (s) ν(OCO)$_{asy}$, 1602 (w), 1571 (s), 1559 (s), 1505 (s), 1492 (w), 1461 (w), 1395 (vs) ν(OCO)$_{sy}$, 1352 (w), 1280 (m), 1232 (m), 1191 (w), 1146 (m), 1088 (m), 975 (w), 878 (w), 828 (vs), 814 (m), 764 (vs), 688 (s), 653 (vs), 630 (w). ^{1}H NMR ($CDCl_3$): δ = 13.85 (s, 1H, OH), 8.84 (s, 1H, C(*H*)N), 8.19 (s, 1H, ArH), 8.16 (d,^{3}J(^{1}H-^{1}H) = 9.0 Hz, 1H, ArH), 7.97 (d,^{3}J(^{1}H-^{1}H) = 7.5 Hz, 1H, ArH), 7.67 (m, 2H, ArH), 7.59 (m, 1H, ArH), 7.45 (m, 2H, ArH), 7.28 (m, 3H, ArH), 1.79 (m, 6H, *n*-Bu-1), 1.47 (m, 12H, *n*-Bu-2/3), 1.02 (t, 9H, *n*-Bu-4) ppm. ^{13}C NMR ($CDCl_3$): δ = 172.59 (COO), 163.85 (COH), 161.82 (d,^{1}J(^{13}C-^{19}F) = 245 Hz), 161.74 (C(*H*)N), 151.72, 145.82, 143.92, 131.41, 130.84, 129.79, 129.26, 128.85, 127.23, 122.62 (d,^{3}J(^{13}C-^{19}F) = 9 Hz), 118.63, 117.97, 117.61 (ArC), 116.32 (d,^{2}J(^{13}C-^{19}F) = 23 Hz), 27.81 (^{2}J(^{13}C-^{119}Sn) = 21 Hz, *n*-Bu-2), 27.04 (^{3}J(^{13}C-^{119}Sn) = 67 Hz, *n*-Bu-3), 16.63 (^{1}J(^{13}C-$^{117/119}$Sn) = 339/356 Hz, *n*-Bu-1), 13.60 (*n*-Bu-4) ppm. ^{19}F NMR ($CDCl_3$); δ = − 114.7 ppm. ^{119}Sn NMR ($CDCl_3$); δ = +110.1 ppm. Electronic absorption data (DMSO, λ_{max}[nm]; ε(M^{-1} cm^{-1}): 326, 2060. HRMS-ESI^{+} (*m/z*, %): found 291.0851 (10), calcd. For [Bu$_3$Sn]$^{+}$ 291.1135; found 625.1638 (100), calcd. For [(Bu$_3$Sn)$_2$CO$_2$H] $^{+}$ 625.2240; found 654.2044 (0.82), calc for [M + H]$^{+}$ 654.2154.

2.4.3. Synthesis of [n-Bu$_3$Sn(HL$^{2\text{-}CF3}$)]$_n$ (3)

An analogous method to that used for preparing compound **1** was

employed, utilizing (n-$Bu_3Sn)_2O$ (0.144 g, 0.24 mmol) and H'$HL^{2\text{-}CF3}$ (0.20 g, 0.48 mmol). Following the workup, crystallization from anhydrous hexane and slow evaporation at room temperature resulted in the formation of orange crystals of compound **3**. Yield: 0.19 g (57 %), M.p.: 93–94 °C. FT-IR (ATR mode; ν in cm^{-1}): 2921 (w) ν(C-H)$_{aliphatic}$, 1655 (s) $\nu(OCO)_{asy}$, 1616 (s), 1597 (s), 1579 (s) 1559 (s), 1484 (m), 1459 (m), 1391 (s) $\nu(OCO)_{sy}$, 1358 (m), 1315 (s), 1282 (m), 1270 (w), 1206 (w), 1158 (m), 1123 (m), 1111 (s), 1088 (m), 1037 (s), 896 (w), 876 (w), 837 (w), 812 (w), 767 (s), 752 (vs), 696 (w), 665 (vs). ^{1}H NMR ($CDCl_3$): δ = 13.07 (s, 1H, OH), 8.63 (s, 1H, C(*H*)N), 8.00 (s, 1H, ArH), 7.97 (d,^3J(^{1}H-^{1}H) = 9.0 Hz, 1H, ArH), 7.75 (d,^3J(^{1}H-^{1}H) = 7.0 Hz, 1H, ArH), 7.69 (d,^3J(^{1}H-^{1}H) = 7.7 Hz, 1H, ArH), 7.58 (t,^3J(^{1}H-^{1}H) = 7.7 Hz, 1H, ArH), 7.44 (m, 2H, ArH), 7.36 (m, 2H, ArH), 7.20 (d, 1H, ArH), 7.08 (d,^3J(^{1}H-^{1}H) = 9.0 Hz, 1H, ArH), 1.54 (m, 6H, *n*-Bu-1), 1.24 (m, 12H, *n*-Bu-2/3), 0.78 (t, 9H, *n*-Bu-4) ppm. ^{13}C NMR ($CDCl_3$): δ = 172.58 (COO), 163.85 (COH), 163.61 (C(*H*)N), 151.79, 146.48, 145.90, 133.24, 131.43, 130.86, 129.84, 129.34, 129.31, 127.86, 126.74, 126.68 (q,^3J(^{13}C-^{19}F) = 8 Hz), 124.25 (q,^2J(^{13}C-^{19}F) = 30 Hz), 123.72 (q,^1J(^{13}C-^{19}F) = 273 Hz, CF_3), 119.30, 118.60, 118.26, 117.66 (ArC), 27.81 (^2J(^{13}C-^{119}Sn) = 20 Hz, *n*-Bu-2), 27.04 (^3J(^{13}C-^{119}Sn) = 66 Hz, *n*-Bu-3), 16.66 (^1J(^{13}C-$^{117/119}$Sn) = 340/355 Hz, *n*-Bu-1), 13.57 (*n*-Bu-4) ppm. ^{19}F NMR ($CDCl_3$); δ = − 60.5 ppm. ^{119}Sn NMR ($CDCl_3$); δ = +110.1 ppm. Electronic absorption data (DMSO, λ_{max}[nm]; ε(M^{-1} cm^{-1}): 331, 1390. HRMS-ESI$^+$ (*m/z*, %): found 291.1097 (42), calcd. For $[Bu_3Sn]^+$ 291.1135; found 625.2126 (78), calcd. For $[(Bu_3Sn)_2CO_2H]^+$ 625.2240.

2.4.4. Synthesis of [n-$Bu_3Sn(HL^{3\text{-}CF3})]_n$ (4)

An analogous method to that used for preparing compound **1** was employed, utilizing (n-$Bu_3Sn)_2O$ (0.144 g, 0.24 mmol) and H'$HL^{3\text{-}CF3}$ (0.20 g, 0.48 mmol). Following the workup, crystallization from anhydrous dichloromethane/hexane (1/1, *v/v*) and slow evaporation at room temperature resulted in the formation of orange crystals of compound **4**. Yield: 0.21 g (60 %), M.p.: 100–101 °C. FT-IR (ATR mode; ν in cm^{-1}): 2921 (w) ν(C-H)$_{aliphatic}$, 1655 (s) $\nu(OCO)_{asy}$, 1616 (s), 1597 (s), 1579 (s), 1558 (s), 1484 (m), 1459 (m), 1391 (s) $\nu(OCO)_{sy}$, 1358 (m), 1315 (s), 1282 (m), 1206 (w), 1158 (m), 1123 (m), 1111 (s), 1088 (m), 1057 (s), 1030 (m), 896 (w), 876 (w), 837 (w), 812 (w), 752 (s), 696 (w), 665 (vs). ^{1}H NMR ($CDCl_3$): δ = 13.41 (s, 1H, OH), 8.75 (s, 1H, C(*H*)N), 8.08 (s, 1H, ArH), 8.04 (d,^3J(^{1}H-^{1}H) = 9.0 Hz, 1H, ArH), 7.83 (d,^3J(^{1}H-^{1}H) = 7.5 Hz, 1H, ArH), 7.58 (m, 3H, ArH), 7.50 (m, 4H, ArH), 7.37 (s, 2H, ArH), 7.15 (d,^3J(^{1}H-^{1}H) = 9.0 Hz, 1H, ArH), 1.62 (m, 6H, *n*-Bu-1), 1.32 (m, 12H, *n*-Bu-2/3), 0.86 (t, 9H, *n*-Bu-4) ppm. ^{13}C NMR ($CDCl_3$): δ = 172.59 (COO), 163.82 (C(*H*)N), 163.64 (COH), 151.64, 148.50, 145.90, 131.99 (q,^2J(^{13}C-^{19}F) = 32 Hz), 131.52, 130.86, 130.11, 129.79, 129.37, 129.11, 128.28, 127.81, 124.49, 123.74 (q,^3J(^{13}C-^{19}F) = 4 Hz), 123.69 (q,^1J(^{13}C-^{19}F) = 272 Hz, CF_3), 118.44, 118.10, 117.58 (ArC), 27.79 (^2J(^{13}C-^{119}Sn) = 21 Hz, *n*-Bu-2), 27.04 (^3J(^{13}C-^{119}Sn) = 65 Hz, *n*-Bu-3), 16.64 (^1J(^{13}C-$^{117/119}$Sn) = 339/355 Hz, *n*-Bu-1), 13.59 (*n*-Bu-4) ppm. ^{19}F NMR ($CDCl_3$); δ = − 62.8 ppm. ^{119}Sn NMR ($CDCl_3$); δ = +110.0 ppm. Electronic absorption data (DMSO, λ_{max}[nm]; ε(M^{-1} cm^{-1}): 321, 1316. HRMS-ESI$^+$ (*m/z*, %): found 291.0917 (100), calcd. For $[Bu_3Sn]^+$ 291.1135; found 625.1729 (30), calcd. For $[(Bu_3Sn)_2CO_2H]^+$ 625.2240; found 704.2490 (0.76), calc for $[M + H]^+$ 704.2122.

2.4.5. Synthesis of [n-$Bu_3Sn(HL^{4\text{-}CF3})]_n$ (5)

An analogous method to that used for preparing compound **1** was employed, utilizing (n-$Bu_3Sn)_2O$ (0.144 g, 0.24 mmol) and H'$HL^{4\text{-}CF3}$ (0.20 g, 0.48 mmol). Following the workup, crystallization from anhydrous ethanol/hexane (2/1, *v/v*) and slow evaporation at room temperature resulted in the formation of orange crystals of compound **5**. Yield: 0.21 g (60 %), M.p.: 98–99 °C. FT-IR (ATR mode; ν in cm^{-1}): 2925 (w) ν(C-H)$_{aliphatic}$, 1624 (w) $\nu(OCO)_{asy}$, 1600 (s), 1573 (vs), 1492 (w), 1463 (w), 1395 (vs) $\nu(OCO)_{sy}$, 1350 (w), 1319 (vs), 1282 (m), 1247 (w), 1216 (w), 1160 (m), 1127 (s), 1103 (s), 1090 (m), 1063 (s), 1010 (m), 975 (w), 896 (m), 880 (m), 847 (s), 820 (s), 767 (vs), 694 (s), 665 (s). ^{1}H NMR ($CDCl_3$): δ = 13.37 (s, 1H, OH), 8.72 (s, 1H, C(*H*)N), 8.06 (s, 1H, ArH), 8.04 (d,^3J(^{1}H-^{1}H) = 9.0 Hz, 1H, ArH), 7.83 (d,^3J(^{1}H-^{1}H) = 7.5 Hz, 1H, ArH), 7.71 (d,^3J(^{1}H-^{1}H) = 8.0 Hz, 2H, ArH), 7.48 (m, 3H, ArH), 7.38 (d,^3J(^{1}H-^{1}H) = 8.0 Hz, 2H, ArH), 7.14 (d,^3J(^{1}H-^{1}H) = 9.0 Hz, 1H, ArH), 1.63 (m, 6H, *n*-Bu-1), 1.32 (m, 12H, *n*-Bu-2/3), 0.87 (t, 9H, *n*-Bu-4) ppm. ^{13}C NMR ($CDCl_3$): δ = 172.57 (COO), 163.94 (C(*H*)N and COH), 151.63, 150.96, 145.90, 131.54, 130.84, 129.80, 129.38, 129.58 (q,^2J(^{13}C-^{19}F) = 33 Hz), 129.27, 127.77, 126.68 (q,^3J(^{13}C-^{19}F) = 4 Hz), 123.95 (q,^1J(^{13}C-^{19}F) = 272 Hz, CF_3), 121.45, 118.44, 118.11, 117.55, 114.04 (ArC), 27.79 (^2J(^{13}C-^{119}Sn) = 20 Hz, *n*-Bu-2), 27.02 (^3J(^{13}C-^{119}Sn) = 63 Hz, *n*-Bu-3), 16.64 (^1J(^{13}C-$^{117/119}$Sn) = 340/356 Hz, *n*-Bu-1), 13.57 (*n*-Bu-4) ppm. ^{19}F NMR ($CDCl_3$); δ = − 62.3 ppm. ^{119}Sn NMR ($CDCl_3$); δ = +110.1 ppm. Electronic absorption data (DMSO, λ_{max}[nm]; ε(M^{-1} cm^{-1}): 326, 1770. HRMS-ESI$^+$ (*m/z*, %): found 291.1458 (100), calcd. For $[Bu_3Sn]^+$ 291.1135; found 625.3518 (3.54), calcd. For $[(Bu_3Sn)_2CO_2H]^+$ 625.2240; found 704.3355 (0.33), calc for $[M + H]^+$ 704.2122.

IR (signal intensity): s, strong; vs, very strong; m, medium; w, weak; br, broad.

NMR (signal multiplicity): s, singlet; d, doublet; t, triplet; m, multiplet.

2.5. X-ray crystallography

Crystals of the pro-ligand H'$HL^{3\text{-}CF3}$ and tri-*n*-butyltin complexes **2**, **4** and **5** were obtained from the following solvent systems [H'$HL^{3\text{-}CF3}$: toluene, **2**: hexane, **4**: dichloromethane/hexane (2:1, *v/v*), **5**: hexane/ethanol (2:1, v/v)]. Suitable specimens of H'$HL^{3\text{-}CF3}$, **2**, and **5** were mounted from oil (polyisobutene) on nylon-loop mounting pins, while that of **4** used a fine glass fibre-mounting pin [67]. X-ray diffraction data were collected at 100.0(2) K using a Bruker D8 Venture dual-source diffractometer with either Mo*Kα* radiation (λ = 0.71073 Å) for H'$HL^{3\text{-}CF3}$, **2**, **5**, or Cu*Kα* radiation (λ = 1.54178 Å) for **4**. Data collection, integration, scaling/merging [68], absorption correction [69,70], and validation [71,72] were all performed using published software. All four structures were solved by the dual-space methods in *SHELXT* [73] and refined by full-matrix least-squares optimization using *SHELXL* [74]. The crystal of **4** was twinned by reticular pseudo-merohedry [75,76] corresponding to a 2-fold rotation about its crystallographic *a*-axis, with a major-to-minor component volume ratio of ~9:1.

2.6. Solubility and stability assessment of tri-n-butyltin compounds 1–5

The tri-*n*-butyltin compounds **1**–**5** are soluble in common solvents but insoluble in water. To ensure drug stability for *in vitro* and *in vivo* applications, organotin(IV) compounds are typically dissolved in DMSO and diluted with a test medium. The stability of the pro-ligands (H'HL^{H}, H'$HL^{4\text{-}F}$, H'$HL^{2\text{-}CF3}$, H'$HL^{3\text{-}CF3}$ and H'$HL^{4\text{-}CF3}$) and their tri-*n*-butyltin derivatives **1–5** was assessed using UV–visible spectroscopy in DMSO, showing stable absorption spectra over 23 days (ESI Figs. S1-S2). For hydrolytic stability studies, the most active compound **2** was dissolved in DMSO at 1×10^{-4} M and diluted with distilled water to 1×10^{-6} M in buffer solution at pH 7.2. UV–vis spectra were recorded immediately and after 72 h (ESI Figs. S3). No decomposition was observed during the study.

2.7. Experimental protocol and anti-proliferative activity tests

2.7.1. Cell line culture and experimental setup

The MDA-MB-231 (breast cancer cells) and HEK-293 (normal human embryonic kidney cells) were cultured in DMEM medium, supplemented with 10 % heat-inactivated FBS and an antibiotic solution. Penicillin-streptomycin solution was added, and the cells were maintained at 37 °C in a humidified atmosphere with 5 % CO_2. Cells were harvested when they reached 80 % confluence and then plated for subsequent experiments.

The tri-*n*-butyltin compounds **1**–**5** (test compounds), pro-ligands (H'HL^{H}, H'$HL^{4\text{-}F}$, H'$HL^{2\text{-}CF3}$, H'$HL^{3\text{-}CF3}$ and H'$HL^{4\text{-}CF3}$) and tri-*n*-

butyltin precursor (tin control: *n*-Bu_3SnCl, were initially prepared as 100 mM stock solutions in DMSO and stored at 4 °C for later use. These stock solutions were diluted to appropriate working concentrations with DMEM for subsequent experiments, ensuring that the final DMSO concentration did not exceed 0.1 %. The CDDP stock solution was prepared at a concentration of 1 mM in a normal saline aqueous solution containing 0.9 % sodium chloride.

2.7.2. Anti-proliferative assays and determination of IC_{50} values

The inhibitory activity of the test compounds was assessed using the MTT assay, which measures cell viability by detecting the conversion of the yellow tetrazolium salt to purple formazan through mitochondrial dehydrogenase activity [77]. Test compounds **1**–**5** were evaluated for cytotoxicity against MDA-MB-231 cancer cells, and normal HEK-293 cells at different concentrations. Pro-ligands**,** as well as the tin control (*n*-Bu_3SnCl) and CDDP, were also tested for comparison.

Approximately 1×10^4 cells/well were seeded in three separate sterile 96-well microplates with complete medium and incubated at 37 °C for 24 h to ensure cell adherence. The cells were treated with different concentrations (0.1 μM, 0.5 μM, 1 μM, 5 μM, 10 μM, 20 μM, and 40 μM) of test compounds and the tin control, while the pro-ligands were tested at concentrations of 0.5 μM, 1 μM, 5 μM, 10 μM, 20 μM, and 40 μM. After a 24-h incubation in a humidified CO_2 incubator, the treatment medium was removed, and 100 μL of freshly prepared medium containing MTT solution (derived from a stock solution of 5 mg mL^{-1}) was added to each well. After two hours of incubation at 37 °C, the MTT-containing medium was replaced with 100 μL of DMSO, followed by an additional 30-min incubation. The absorbance was then measured at 570 nm using a microplate reader. All experiments were performed concurrently in triplicate. Anti-proliferative activities of the test and tin control were quantified as the percentage of reduced cell growth, expressed as Cell viability (%) = (Absorbance of treated cells / Absorbance of control cells) × 100. The IC_{50} value was determined to assess the effectiveness of the test compounds, representing the concentration causing 50 % inhibition of cell growth, and expressed as the mean ± SEM. Further experiments with MDA-MB-231 cancer cells were continued because compound **2** was effective, showing significant cytotoxicity with minimal effects on normal cells, while compounds **1** and **3**–**5** exhibited high cytotoxicity in MDA-MB-231 cells.

2.7.3. Detection of apoptosis using acridine orange/ethidium bromide (AO/EB) dual staining assay

Acridine orange/ethidium bromide (AO/EB) staining, observed under a fluorescence microscope, can identify apoptosis-related membrane changes and clearly distinguish between normal cells, early apoptotic cells, late apoptotic cells, and necrotic cells [78]. AO penetrates the plasma membrane and binds to the DNA of live cells, emitting a green fluorescence, while EB selectively stains the DNA of dead cells, producing a red-orange fluorescence. For the experiment, MDA-MB-231 and cells (5×10^4 cells per well) were seeded into sterile 12-well culture plates and allowed to adhere overnight in a humidified CO_2 incubator at 37 °C. The cells were treated with concentrations of test compound **2** close to its IC_{50}, including lower (0.3 μM), IC_{50} (0.9 μM), and higher (1.2 μM) concentrations. Additionally, cells were treated with the pro-ligand $H'HL^{4\text{-}F}$ at a concentration of 0.9 μM as a reference compound for comparison. After 24 h of treatment, the cells were rinsed with PBS and separately stained with AO and EtBr at a concentration of 10 μg/mL. Following two washes with PBS and a 30-min incubation at 37 °C, images were captured in both the green and red fluorescence channels using an inverted fluorescence microscope. All experiments were carried out simultaneously and in triplicate.

2.7.4. Reactive oxygen species (ROS) generation assay

Elevated levels of ROS signal that cells are under stress and having difficulty performing their normal functions. ROS levels can be assessed by treating both test and reference compounds with DCFH-DA, followed by fluorescence measurement. The assay was conducted using the most potent test compound, **2**, to investigate its influence on ROS production in MDA-MB-231 and cells [64,65]. In brief, MDA-MB-231 cells (5×10^4) were seeded into sterile 12-well culture plates and then incubated at 37 °C for 24 h. After treatment, the culture media were removed, and the wells were rinsed with PBS. The cells were treated with concentrations of test compound **2** near its IC_{50} (lower (0.3 μM), IC_{50} (0.9 μM), and higher (1.2 μM)) concentration, along with the reference pro-ligand $H'HL^{4\text{-}F}$ at 0.9 μM for comparison. After an additional 24-h incubation period, both the treated and the control cells were washed with PBS. The cells were then stained with 10 μM DCFH-DA dye for 30 min, followed by two more washes with PBS. The treated and control cells were then analyzed to quantify ROS levels. Fluorescence images were captured in the green channel, along with phase contrast images. All experiments were carried out simultaneously and in triplicate.

2.7.5. Mitochondrial aggregation (MitoTracker)

Different anticancer drugs trigger apoptosis by altering mitochondrial distribution and structure, with pro-apoptotic signals linked to these changes. MitoTracker, a lipophilic cationic dye absorbed by mitochondria, is commonly used to observe mitochondrial fluorescence [79]. To evaluate the distribution pattern of mitochondria, MDA-MB-231 cells (5×10^4 cells/well) were cultured in 12-well plates with complete DMEM and incubated for 24 h. The cells were then exposed to test compound **2** at concentrations near its IC_{50}: (lower (0.3 μM), IC_{50} (0.9 μM), and higher (1.2 μM)), along with the reference pro-ligand $H'HL^{4\text{-}F}$ at 0.9 μM for comparison and further incubated for 24 h. Afterward, the cells were rinsed with PBS and stained with MitoTracker® Red (1 μM) and Hoechst 33342 (10 μg/mL) for 30 min to label mitochondria and nuclei, respectively. Following two PBS washes, cellular morphology was visualized using an inverted fluorescence microscope. Phase-contrast, red (mitochondrial), and blue (nuclear) fluorescence channel images were captured at high magnification for subsequent analysis.

2.7.6. Mitochondrial membrane potential assay

JC-1 dye (5,5′,6,6′-tetrachloro-1,1′,3,3′-tetraethylbenzimidazolylcarbocyanine iodide) is a lipophilic, cationic, and fluorescent dye commonly used to study mitochondrial membrane potential, offering valuable insights into mitochondrial health and activity [80]. In healthy mitochondria, JC-1 forms aggregates that emit red fluorescence. As the membrane potential decreases, JC-1 dissociates into monomers, which emit green fluorescence. The ratio of red to green fluorescence serves as an indicator of mitochondrial condition. To evaluate the mitochondrial membrane potential (MMP), MDA-MB-231 cells (5×10^5 cells/well) were seeded into 12-well culture plates and treated according to the specified protocol to evaluate MMP. The cells were then stained with 1 μM JC-1 dye prepared in PBS and incubated at 37 °C for 30 min. Following incubation, images were captured for analysis.

2.7.7. Cell cycle analysis

Flow cytometry, combined with propidium iodide (PI) labeling, was used to evaluate the effect of test compound **2** and the reference pro-ligand $H'HL^{4\text{-}F}$ on the distribution of MDA-MB-231 cells throughout the cell cycle. Initially, trypsinized cells were plated in 6-well plates and allowed to incubate overnight under humidified conditions. The cells were then treated with test compound **2** at concentrations near its IC_{50}: lower (0.3 μM), IC_{50} (0.9 μM), and higher (1.2 μM)), as well as with the reference pro-ligand $H'HL^{4\text{-}F}$ at 0.9 μM for comparison. Following a 24-h treatment, the cells were harvested using 1.0 mM EDTA and washed twice with PBS at pH 7.4. The cells were fixed in 75 % ice-cold molecular-grade ethanol and stored at −20 °C overnight. Following fixation, the cells were centrifuged to remove the ethanol and stained with a solution containing 20 μg/mL PI, 100 μg/mL RNase A, and 0.1 % Triton-X in PBS. The samples were incubated at 37 °C for 30 min to ensure complete staining. Fluorescence intensity was then measured using a

Beckman Coulter flow cytometer, and the distribution of cells across different phases of the cell cycle (G0/G1, S, and G2/M) was determined by analyzing the resulting histograms.

2.7.8. Statistical analysis

Results are expressed as the mean ± SEM from three independent experiments. Statistical analysis was performed using one-way ANOVA followed by Tukey's post-hoc test, conducted with GraphPad Prism version 8.0.2. A 95 % confidence level was applied, and statistical significance was indicated as * for *p*-values less than 0.05.

3. Results and discussion

3.1. Design aspects, synthesis and spectroscopic characterization

The pre-ligand, 2-[(*E*)-2-(3-formyl-4-hydroxyphenyl)-1-diazenyl] benzoic acid (H'HL), was synthesized through a diazo-coupling reaction between anthranilic acid and salicylaldehyde [66]. This compound serves as an excellent precursor for further functionalization, allowing it to undergo subsequent reactions with suitable amines to yield Schiff bases with the desired functional or donor groups [45–53]. When the pre-ligand was reacted with aniline, 4-fluoroaniline, 2-(trifluoromethyl) aniline, 3-(trifluoromethyl)aniline, and 4-(trifluoromethyl)aniline, several hydroxy-benzoic acid pro-ligands were obtained. These pro-ligands feature potential metal-coordinating functional groups separated by a semi-rigid aromatic azomethine- and diaza- scaffold with varying steric hindrance. The pro-ligands, designated as H'HL^{H}, H'HL$^{4\text{-}F}$, H'HL$^{2\text{-}CF3}$, H'HL$^{3\text{-}CF3}$ and H'HL$^{4\text{-}CF3}$, were then reacted with bis(tri-*n*-butyltin)oxide, resulting in five complexes: [*n*-Bu$_3$Sn(HL^{H})] (**1**), [*n*-Bu$_3$Sn(HL$^{4\text{-}F}$)]$_n$ (**2**), [*n*-Bu$_3$Sn(HL$^{2\text{-}CF3}$)]$_n$ (**3**), [*n*-Bu$_3$Sn(HL$^{3\text{-}CF3}$)] (**4**) and [*n*-Bu$_3$Sn(HL$^{4\text{-}CF3}$)] (**5**) (Scheme 2). The reactions proceeded smoothly in anhydrous toluene after water removal, with final product yields exceeding 55 %, depending on the purification/ workup procedures and crystal recovery conditions. Compounds **1**–**5** are orange crystalline solids with distinct melting points ranging from 93 to 122 °C. Crystalline samples of compounds **1**–**5** can be stored in an inert environment for several months, retaining their colour, luster, and melting points. They demonstrate significant stability in both their solid form and when

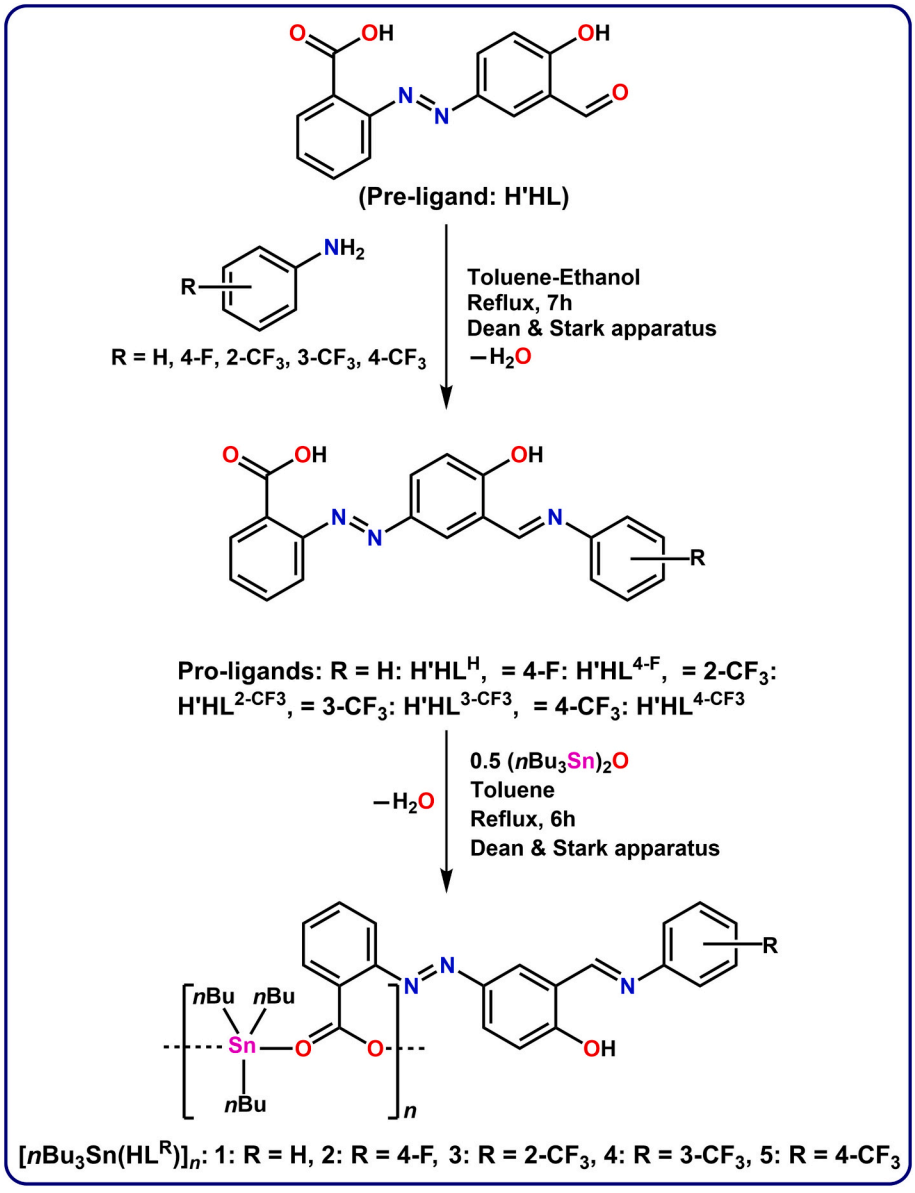

Scheme 2. Reaction sequences for synthesizing the pro-ligands (H'HL^{H}, H'HL$^{4\text{-}F}$, H'HL$^{2\text{-}CF3}$, H'HL$^{3\text{-}CF3}$ and H'HL$^{4\text{-}CF3}$, where H and H′ represent hydroxyl and carboxylic acid protons, respectively, and their tri-*n*-butyltin compounds **1**–**5**.

dissolved in solution, as confirmed by SC-XRD analysis, ^{119}Sn NMR, and electronic spectral studies. Pro-ligands and compounds **1**–**5** were characterized by FT-IR (ATR) spectroscopy (ESI Figs. S4-S13), NMR (^{1}H, ^{13}C and ^{19}F) (ESI Figs. S14-S41), ^{119}Sn NMR (ESI Figs. S42-S46), and HRMS (ESI Figs. S47-S51).

Post-synthesis, single crystals of compounds **2**, **4** and **5** were isolated via recrystallization, enabling determination of their crystal and molecular structures in the solid state. The solid-state structures of compounds **2**, **4,** and **5**, as well as the pro-ligands, H'HL$^{3\text{-CF3}}$, were determined by single-crystal X-ray diffraction studies.

Diagnostically useful FT-IR absorptions are provided in the Experimental section. The FT-IR spectra of compounds **1**–**5** were compared to those of the pro-ligands (H'HL^{H}, H'HL$^{4\text{-F}}$, H'HL$^{2\text{-CF3}}$, H'HL$^{3\text{-CF3}}$, and H'HL$^{4\text{-CF3}}$) to examine the coordination behavior of the carboxylic group. The characteristic ν(OH)$_{phenolic}$ and ν(OH)$_{carboxylic}$ bands could not be distinctly assigned in the spectra, as these bands typically appear broad and weak, likely being obscured beneath the baseline noise. However, the presence of OH groups has been confirmed from the results of the ^{1}H NMR and diffraction data (vide infra). The pro-ligands exhibit a moderately intense absorption band between 1721 and 1730 cm^{-1}, corresponding to ν(COO)$_{asy}$. In the tri-*n*-butyltin compounds **1**–**5**, this band shifts to the range of 1614–1624 cm^{-1}. This shift suggests the deprotonation of the carboxylic acid group and implies a C=O → Sn interaction upon complexation. The FT-IR spectra of compounds **1**–**5** show bands at around 1391–1396 cm^{-1}, corresponding to the ν(COO)$_{sy}$ vibration frequencies of the COO^{-} group. The $\Delta\nu$ value ($\Delta\nu = \nu(COO)_{asy} - \nu(COO)_{sy}$) ranges from 223 to 228 cm^{-1}, indicating a monodentate coordination mode for the carboxylate ligand [81]. Although this value falls within the typical range for monodentate coordination ($\Delta\nu \geq 200$ cm^{-1}), it also suggests a possible borderline case for chelating bidentate or anisobidentate coordination [81]. This ambiguity was ultimately clarified through X-ray single-crystal analysis of compounds **2, 4** and **5** (vide infra). Additionally, the IR spectra of compounds **1**–**5** display characteristic bands at 2925 cm^{-1} corresponding to ν(C-H)$_{aliphatic}$ of the Sn-Bu group [82]. Overall, the pro-ligands did not show a proton signal for the carboxylic acid, possibly due to exchange effects caused by the presence of water in the solvent. In addition, the ^{1}H, ^{13}C and ^{19}F NMR spectra of the pro-ligands and their compounds **1**–**5** (ESI Figs. S14-S41), along with the ^{119}Sn NMR data for compounds **2**–**5** (ESI Figs. S42-S45), displayed the expected resonances corresponding to the anticipated structures. Both the pro-ligands (except H'HL$^{4\text{-F}}$) and the tri-*n*-butyltin compounds **1**–**5** displayed a singlet in the range 13.07 to 14.46 ppm, attributed to phenolic OH, as well as a singlet between 8.63 and 8.84 ppm, assigned to the C(*H*)N azomethine group. The carboxylic carbon signal of free pro-ligands were observed in the range of 164–169 ppm, while in compounds **1**–**5**, this signal appeared around 172 ppm. This downfield shift of the signal can be attributed to the coordination of the carboxylate group to the tin atom. Additionally, the ^{1}H and ^{13}C NMR spectra of compounds **1**–**5** in $CDCl_3$ display distinct signal patterns in the aromatic region for the ligand and in the aliphatic region for the Sn-Bu group. The presence of a single set of signals further indicates that the Sn-Bu groups are equivalent on the NMR timescale. The ^{1}H and ^{13}C chemical shift assignments for the tri-*n*-butyltin group are clear based on the multiplicity patterns, resonance intensities, and by analyzing the ^{n}J (^{13}C-^{117}/^{119}Sn) coupling constants. Four-coordinated tri-*n*-butyltin compounds typically show ^{1}J(^{13}C-$^{117/119}$Sn) couplings in the range of 325–390 Hz, while five-coordinated compounds exhibit couplings between 440 and 540 Hz [83,84]. In the present study, the tri-*n*-butyltin complexes display ^{1}J(^{13}C-$^{117/119}$Sn) coupling satellites in the range of 339–356 Hz in $CDCl_3$ solution, indicating that the tin atom is four-coordinate in solution. Complexes **1**–**5** also show a single sharp ^{119}Sn resonance in the range + 110 to +115 ppm, which aligns with the range typical for tetrahedral tri-*n*-butyltin compounds [84]. This observation further indicates that the polymeric structures of complexes **2**, **4**, and **5**, as revealed by diffraction studies in the solid state (vide infra), dissociate in solution to form four coordinate tin species. This is also corroborated by our recent study on similar tri-*n*-butyltinbenzoates [53,85]. The ^{19}F NMR spectra of pro-ligands H'HL$^{4\text{-F}}$, H'HL$^{2\text{-CF3}}$, H'HL$^{3\text{-CF3}}$, and H'HL$^{4\text{-CF3}}$ in $CDCl_3$ exhibit a sharp singlet at δ −114.9, −60.4, −62.7, and −62.3 ppm, which remain unchanged in their tri-*n*-butyltin derivatives **2**–**5**.

Compounds **1**–**5** were also characterized by HRMS, and the mass-to-charge ratios of the ions were measured in an acetonitrile solution within the range of *m/z* 100–1200 Da. The most relevant mass clusters detected in the experiments are shown in the ESI Figs. S47-S51. In the mass spectra of compounds **1**–**5**, a weak molecular ion peak corresponding to the protonated molecule $[M + H]^{+}$ was observed with m/z values of 654.2044 (0.82 %) for **2**, 704.2490 (0.76 %) for **4**, and 704.3355 (0.33 %) for **5**. The fragmentation patterns of all five compounds also display characteristic peaks at m/z = 291.1 for $[Bu_3Sn]^{+}$, which results from the loss of one mole of ligand from the complex due to cleavage of the weak Sn-O bond [54], and at m/z = 625.2 for $[(Bu_3Sn)_2CO_2 + H]^{+}$.

3.2. Description of the crystal structures

Crystallographic data, along with details of data collection and structure refinement details for the pro-ligand H'HL$^{3\text{-CF3}}$, and the polymeric tri-*n*-butyltin compounds **2**, **4** and **5,** are given in ESI Table S1. Ellipsoid plots of H'HL$^{3\text{-CF3}}$ and compounds **2**, **4** and **5** (whole molecule for H'HL$^{3\text{-CF3}}$ and the asymmetric units for polymers **2**, **4** and **5**) are shown in Fig. 1 (For additional figures, refer to ESI Figs. S52-S62). All bond lengths and angles are within normal ranges and are tabulated in the ESI Tables S2-S13. Selected geometric parameters for compounds **2**, **4**, and **5** are summarized in Table 1.

The pro-ligand H'HL$^{3\text{-CF3}}$ crystallizes with trigonal $R\bar{3}$ symmetry, incorporating channels that extend parallel to the crystallographic *c*-axis (Fig. S53). Such channels are common for this space group and often-incorporate solvent [86], however, for H'HL$^{3\text{-CF3}}$ they are small, allowing negligible (if any) solvent penetration. An electron count within these 'voids' estimated using *Platon* [87] amounted to only ~3e^{-} per unit cell. The molecular structure consists of a benzoic acid group connected at its 2-position via an diazenyl-linker to the 4-position of a phenolic ring, which in turn is connected to the 3-position (*meta*) of a trifluorophenyl group by an imino group. Geometries at the diazenyl- and imino-linkers are both *trans*, giving C3–N1–N2–C8 and C10–C14–N3–C15 torsion angles of −177.75(10)° and 177.59(14)°, respectively (Table 2). Two *intra*-molecular hydrogen bonds [O1–H1…N1, d_{D-A} = 2.6106(18) Å] and [O3–H3…N3, d_{D-A} = 2.6351(18) Å] restrict the conformational flexibility of the molecule (Fig. 1(a)). Torsion angles C3–C2–C1–O1 and C14-C10-C11-O3 being 4.03(2)° and − 1.24 (2)°, respectively. The molecule deviates from planarity largely by twisting about bonds N2–C8 and N3–C15, leading to dihedral angles between the central phenolic ring with benzoic acid and tri-fluorophenyl rings of 15.41(3)° and 20.44(4)°, respectively. The overall r.m.s. deviation from the mean plane passing through all non-H / F atoms is 0.2874 Å (largest deviation = 0.779(2) Å at C21). There are no strong *inter*-molecular hydrogen bonds in crystalline H'HL$^{3\text{-CF3}}$, though the default suggestions for 'potential hydrogen bonds' in *SHELXL* lists a few C–H…O and C–H…F contacts (see Table S4). No π–π stacking between aromatic rings on adjacent molecules is observed, but due to the trigonal symmetry, the molecules stack into columns along the *c*-axis, with each successive molecule rotated by 120°.

The tri-*n*-butyltin compounds **2**, **4**, and **5** form mono-periodic chains, where each *n*-Bu_3Sn unit is connected to benzoic acid oxygen atoms through one short and one long Sn-O bond (Table 1). These compounds, examined in the present study, fall under the broader classification **V**, as shown in Scheme 1. The geometry at the tin atoms in compounds **2**, **4 and 5** is slightly distorted trigonal bipyramidal, as follows from their τ_5 parameters [88], which range from 0.85 (compounds **2** and **5**) to 0.87 and 0.88 (compound **4**). The τ_5 parameter assumes a value of 1 for a

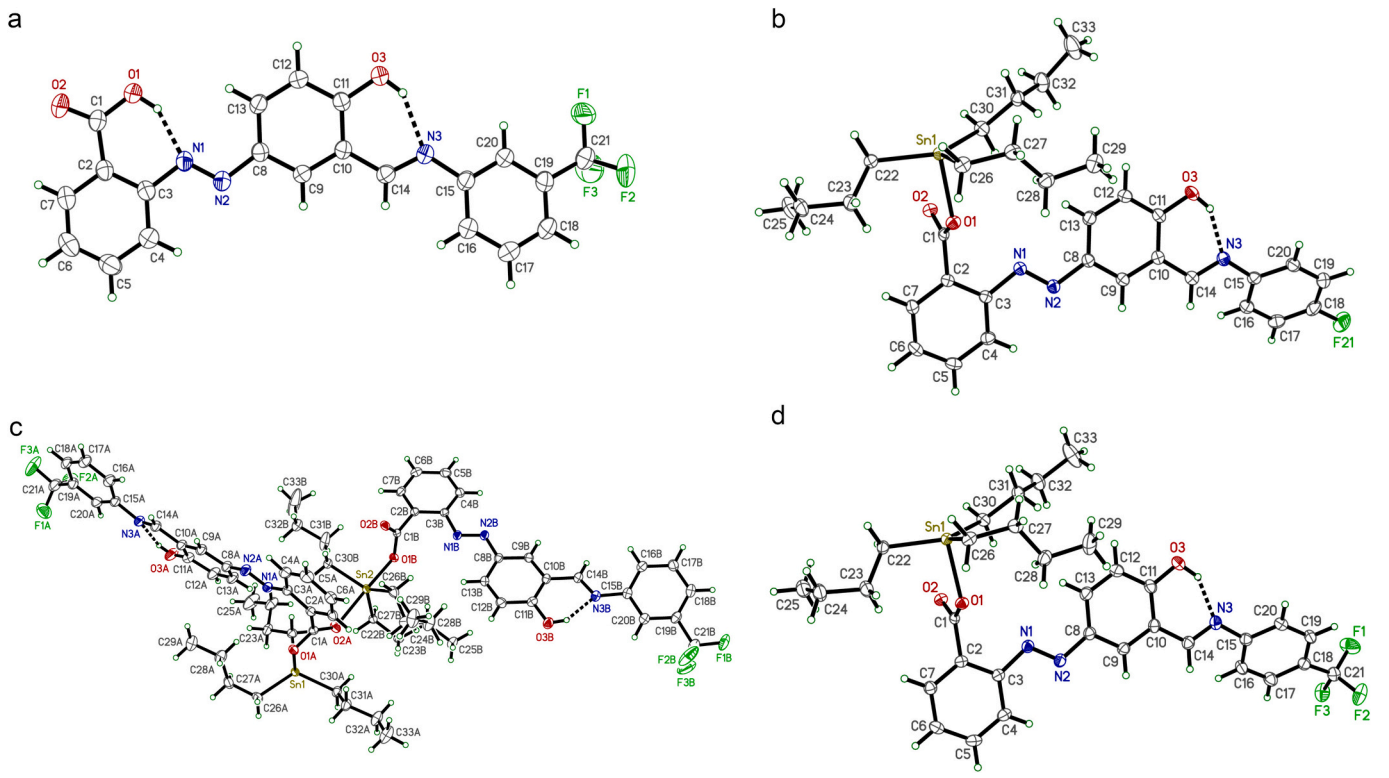

Fig. 1. Ellipsoid plots of pro-ligand (a) H'HL$^{3\text{-}CF3}$, and tri-*n*-butyltin compounds (b) **2**, (c) **4**, and (d) **5**, all drawn at 50 % probability. Hydrogen atoms are shown as small arbitrary circles. For the sake of clarity, only the major components of *n*-Bu-group disorder in **2** and **4** are shown.

Table 1
Selected bond lengths and angles (Å, °) in tri-*n*-butyltin compounds **2**, **4**, and **5**.

	2	**4**	**5**
Distances[a]			
Sn1-O1	2.2147(10)	2.2134(16)	2.2059(10)
Sn2-O1(B)	–	2.2144(17)	–
Sn1-O2^{sym}	2.4342(10)	2.4531(16)	2.4336(10)
Sn2-O2(A)	–	2.4276(17)	–
Sn1-C22(A)	2.1351(14)	2.144(2)	2.1440(15)
Sn2-C22(B)	–	2.149(2)	–
Sn1-C26(A)	2.1473(14)	2.148(3)	2.1437(14)
Sn2-C26(B)	–	2.147(3)	–
Sn1-C30(A)	2.1435(14)	2.139(2)	2.1434(15)
Sn2-C30(B)	–	2.139(3)	–
Angles[a]			
O1(A)-Sn1-O2(B)^{sym}	173.60(3)	174.28(6)	172.62(4)
O1(B)-Sn2-O2(A)		173.92(6)	–
C22(A)-Sn1-C26(A)	115.83(6)	121.73(11)	116.25(6)
C22(B)-Sn2-C26(B)		119.20(9)	–
C26(A)-Sn1-C30(A)	120.78(6)	118.43(10)	120.63(6)
C26(B)-Sn2-C30(B)		121.64(11)	–
C22(A)-Sn1-C30(A)	122.80(6)	118.18(10)	121.81(6)
		117.68(11)	-

[a] Suffixes in parentheses are for compound **4** (Z' = 2: formula units, A & B).
^{sym} Symmetry operations here are **2** (1-*x*, *y*-0.5, 1.5-*z*), **4** (1+*x*, *y*, *z*), **5** (1.5-*x*, 0.5+*y*, 1.5-*z*).

Table 2
Conformation and geometry defining parameters in H'HL$^{3\text{-}CF3}$, **2**, **4**, and **5**.

	H'HL$^{3\text{-}CF3}$	**2**	**4**[a]	**5**
Dihedrals (°)				
∠ L_{Ph1}–L_{Ph2}	15.41(3)	1.79(9)	12.72(14) 2.67(16)	1.16(9)
∠ L_{Ph2}–L_{Ph3}	20.44(4)	34.50(6)	15.73(15)	38.60(6)
	–	–	21.06(13)	-
Torsions (°)				
C3–N1–N2–C8	−177.75 (13)	179.59(11)	178.6(2)	−179.91 (12)
	–	–	−179.08 (18)	–
C10–C14–N3–C15	177.59(14)	−176.11 (13)	−175.5(2)	−174.17 (14)
	–	–	−175.5(2)	–
C3–C2–C1–O1	4.03(2)	−86.03(16)	−67.3(3)	−84.34(17)
	–	–	−80.3(3)	–
C14–C10–C11–O3	−1.24(2)	−0.2(2)	−2.9(4)	0.3(2)
	–	–	1.9(4)	–
Sn geometry				
τ_5	–	0.85	0.88	0.85
		–	0.87	–

L_{Ph1}, L_{Ph2}, L_{Ph3} are the mean planes through benzene rings C2–C7, C8–C13, and C15–C20.
[a] In **4** dihedrals and torsions, upper entry is A, lower is B; for τ_5, upper is Sn1, lower is Sn2.

perfect trigonal bipyramid versus 0 for a square-based pyramid. The complexes differ chemically by the nature and placement of the substituent on the distal phenyl ring. In **2**, a fluorine atom is located at the 4-position (i.e., *para*), while compounds **4** and **5** carry –CF_3 groups at the 3-position (*meta* as in H'HL$^{3\text{-}CF3}$) and 4-position (*para*), respectively. The pro-ligands for compounds **2** and **5** (i.e., H'HL$^{4\text{-}F}$ and H'HL$^{4\text{-}CF3}$) currently remain unpublished. The asymmetric units of the polymeric structures **2**, **4** and **5** are shown in Fig. 1(b-d). Although the manner in which these polymer chains propagate via –O–Sn-O– linkages are similar, the asymmetric units of compounds **2** and **5** comprise a single [*n*-Bu_3Sn(HL$^{4\text{-}F}$)] or [*n*-Bu_3Sn(HL$^{4\text{-}CF3}$)] segment, while that of

compound **4** comprises two [*n*-$Bu_3Sn(HL^{3\text{-}CF3})$] segments (suffixed as A and B). In compound **4**, the most substantial change in ligand geometry relative to its pro-ligand ($H'HL^{3\text{-}CF3}$) lies in the torsion of the benzoic acid ring and carboxylate groups. In $H'HL^{3\text{-}CF3}$ these are largely co-planar due to the *intra*-molecular O1–H1…N1 hydrogen bond (vide supra), whereas in **4**, this constraint is lost upon bonding to Sn1, leading to C3–C2–C1–O1 torsion angles of −67.3(3)° and − 80.3(3)° for the 'A' and 'B' ligands, respectively (Table 2). Although the structures of pro-ligands $H'HL^{4\text{-}F}$ and $H'HL^{4\text{-}CF3}$ are unavailable, analogous O1–H1…N1 intra-molecular hydrogen bonds as in $H'HL^{3\text{-}CF3}$ are a reasonable possibility. Pro-ligand $H'HL^{H}$, however, which includes a similar 2-diazenyl-benzoic acid moiety, does not include an analogous O1–H1…N1 *intra*-molecular hydrogen bond [89]. In the structures of **2** and **5**, the C3–C2–C1–O1 torsion angles deviate substantially from co-planarity at −86.03(16)° and − 84.34(17)°, respectively. These are similar to, but even more exaggerated than in **4**. Other variations in ligand geometry upon Sn-complex formation are less dramatic. The quantified values are shown in Table 2. The three *n*-Bu groups attached to each Sn atom in compounds **2**, **4** and **5** are largely unremarkable. In **2**, one butyl group is disordered over two conformations (occupancy ratio 0.77:0.33) and in **4**, Sn1 has one disordered butyl (ratio 0.80:0.20) while Sn2 has two disordered butyls (ratios 0.76:0.34 and 0.92:0.08). There is no disorder in **5**. The manner in which the polymer chains in compounds **2**, **4** and **5** propagate relative to their respective unit cells is shown in Fig. 2. Generic packing plots for each structure viewed down their crystallographic *a*, *b*, and *c*-axes are provided in the ESI Figs. S52–62.

3.3. Anti-proliferative effects, mechanism of cell death, and generation of reactive oxygen species

3.3.1. Assessment of concentrations that influence cell survival

The MTT assay was conducted on MDA-MB-231 cancer cells and normal HEK-293 cells to evaluate the anticancer and cytotoxic effects of test compounds **1**–**5**. Results were compared with their pro-ligands, the tin control (*n*-Bu_3SnCl), untreated controls, and the chemotherapy drug CDDP as a positive control after 24 h of treatment. Compounds **1**–**5** demonstrated significant cytotoxicity against MDA-MB-231 cells in a concentration-dependent manner (ESI Fig. S63 (A)), with IC_{50} values provided in Table 3. Among all the tested tin compounds, compound **2**, $[n\text{-}Bu_3Sn(HL^{4\text{-}F})]_n$, exhibited the highest cytotoxicity, displaying an IC_{50} of 0.90 μM. The pro-ligands had no cytotoxic effects, while the tin control *n*-Bu_3SnCl was cytotoxic only at higher concentrations (IC_{50} = 8.50 μM). Both compound **2** and $H'HL^{4\text{-}F}$ displayed minimal toxicity in HEK-293 normal cells, suggesting good selectivity (ESI Fig. S63 (B)). These results indicate that compound **2** exhibits significantly greater cytotoxic efficacy against MDA-MB-231 cells compared to the other compounds. To evaluate its selectivity and biocompatibility, we further tested toxicity of compound **2** against the HEK-293 normal cell line, which show minimal toxicity. Therefore, additional studies were carried out on compound **2**, as it shows promise for further development as a potential treatment for breast cancer.

Table 3
The cytotoxicity (IC_{50} values) of the investigated compounds (tri-*n*-butyltin(IV) compounds **1**–**5**, pro-ligands along with organotin(IV) precursor, *n*-Bu_3SnCl) against breast cancer cells (MDA-MB-231) and normal cells (HEK-293).

Compounds	IC_{50} (μM) ± SEM[a] after 24 h of cells incubation	
	MDA-MB-231 cells	HEK-293 cells
Tri-*n*-butyltin test compounds (**1**–**5**) and pro-ligands ($H'HL^{R}$)		
1	1.50 ± 0.12	–
2	0.90 ± 0.05	33.8 ± 0.26
3	1.54 ± 0.14	–
4	2.18 ± 0.17	–
5	2.07 ± 0.21	–
$H'HL^{H}$	>40	–
$H'HL^{4\text{-}F}$	>40	>40
$H'HL^{2\text{-}CF3}$	>40	–
$H'HL^{3\text{-}CF3}$	>40	–
$H'HL^{4\text{-}CF3}$	>40	–
Organotin control		
n-Bu_3SnCl	8.50 ± 0.19	–
Standard drug		
CDDP	36.70 ± 0.41	–

[a] SEM; Standard error of mean calculated for the average of three sets of independent experiments.

3.3.2. Evaluation of cellular and nuclear morphological alterations during apoptosis

The induction of apoptosis in MDA-MB-231 cells treated with the tin compound **2** and the reference compound $H'HL^{4\text{-}F}$ was assessed using acridine orange/ethidium bromide (AO/EB) dual staining, and the images are displayed in Fig. 3. Microscopic analysis demonstrated a dose-dependent increase in apoptotic cells upon treatment with compound **2**.

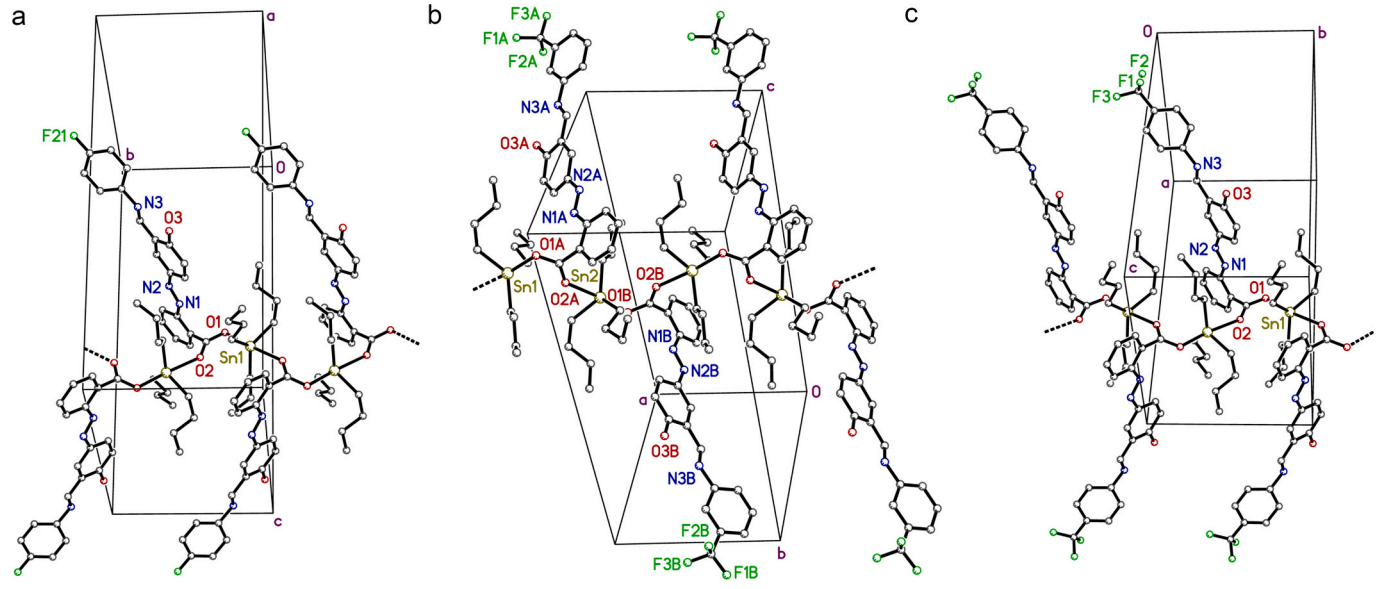

Fig. 2. Partial packing plots showing the propagation of the polymer chains parallel to (a) the *b*-axis of **2**, (b) the *a*-axis of **4**, and (c) the *b*-axis of **5**. Connections to adjacent links in each chain are indicated by dashed lines.

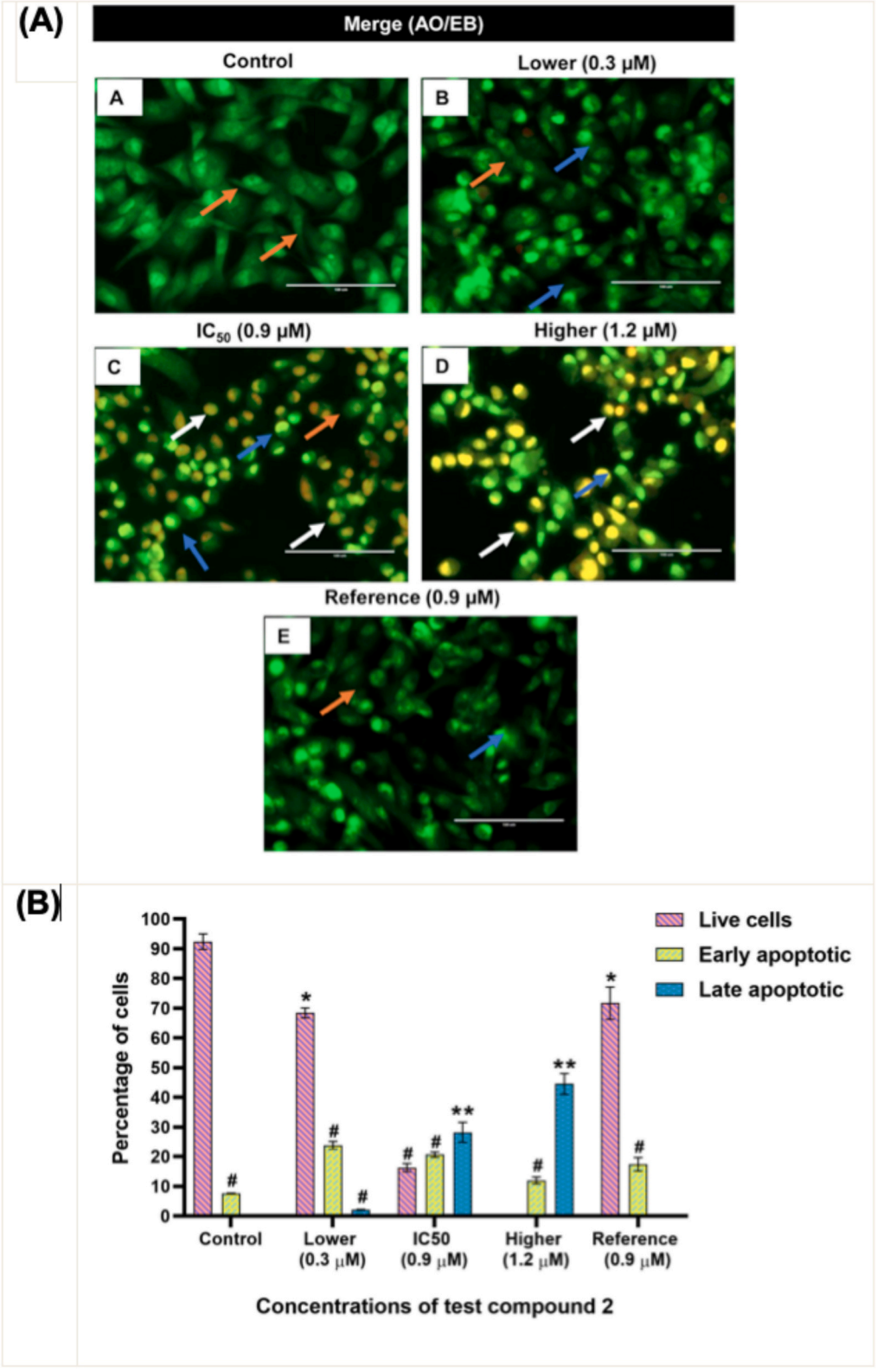

Fig. 3. (**A**) Representative images (Panels A-E) illustrate morphological changes in MDA-MB-231 cells stained with acridine orange/ethidium bromide (AO/EB) fluorescent dye following treatment with various concentrations of test compound **2**, along with the pro-ligand H'HL$^{4\text{-F}}$ used as a reference. The images were captured using a fluorescence microscope. Live cells are indicated by orange arrows, early apoptotic cells by blue arrows, and late apoptotic cells by white arrows. Scale bar: 100 μM; magnification: 400×. (**B**) Graphical illustration depicts the percentage cell viability of MDA-MB-231 cells treated with Compound **2** at concentrations of 0.3, 0.9, and 1.2 μM, compared to untreated controls. Statistical significance was determined using one-way ANOVA followed by Tukey's post hoc test, with thresholds set at $*p < 0.05$, $**p < 0.01$, and $\#p < 0.001$. (For interpretation of the references to colour in this figure legend, the reader is referred to the web version of this article.)

In the untreated control group, cells exhibited light green fluorescence with intact nuclear membranes, consistent with viable cells (92.39 %). Very few cells, however, showed a condensed nucleus with bright green fluorescence, accounting for 7.6 % of the cell population. In contrast, cells treated with compound **2** resulted in distinct apoptotic features, including bright green nuclei with condensed chromatin, a distinct characteristic of early apoptosis, alongside orange-stained fragmented chromatin, characteristic of late apoptotic stages. As shown in Fig. 3, treatments with compound **2** at its IC_{50} (0.9 μM) and at a higher concentration (1.2 μM) induced both early and late apoptotic features. At IC_{50} (0.9 μM) concentration, the early and late apoptotic cell population was increased to 26.65 and 28.26 % respectively. Conversely, the lower concentration (0.3 μM) produced no significant morphological changes compared to the control, which accounts for 23.91 % of the cell population having condensed nuclei. Whereas in case of cells treated with a higher concentration (1.2 μM), only early (11.95 %) and late apoptotic cells (44.56 %) were found with reduced cell viability. These apoptotic features were more pronounced in cells treated with compound **2** than in those exposed to the reference compound $H'HL^{4\text{-}F}$, which exhibited no sign of apoptotic features under comparable conditions [90]. Overall, these findings suggest that compound **2** possesses stronger pro-apoptotic activity than $H'HL^{4\text{-}F}$. Its effects are dose-dependent, with increasing

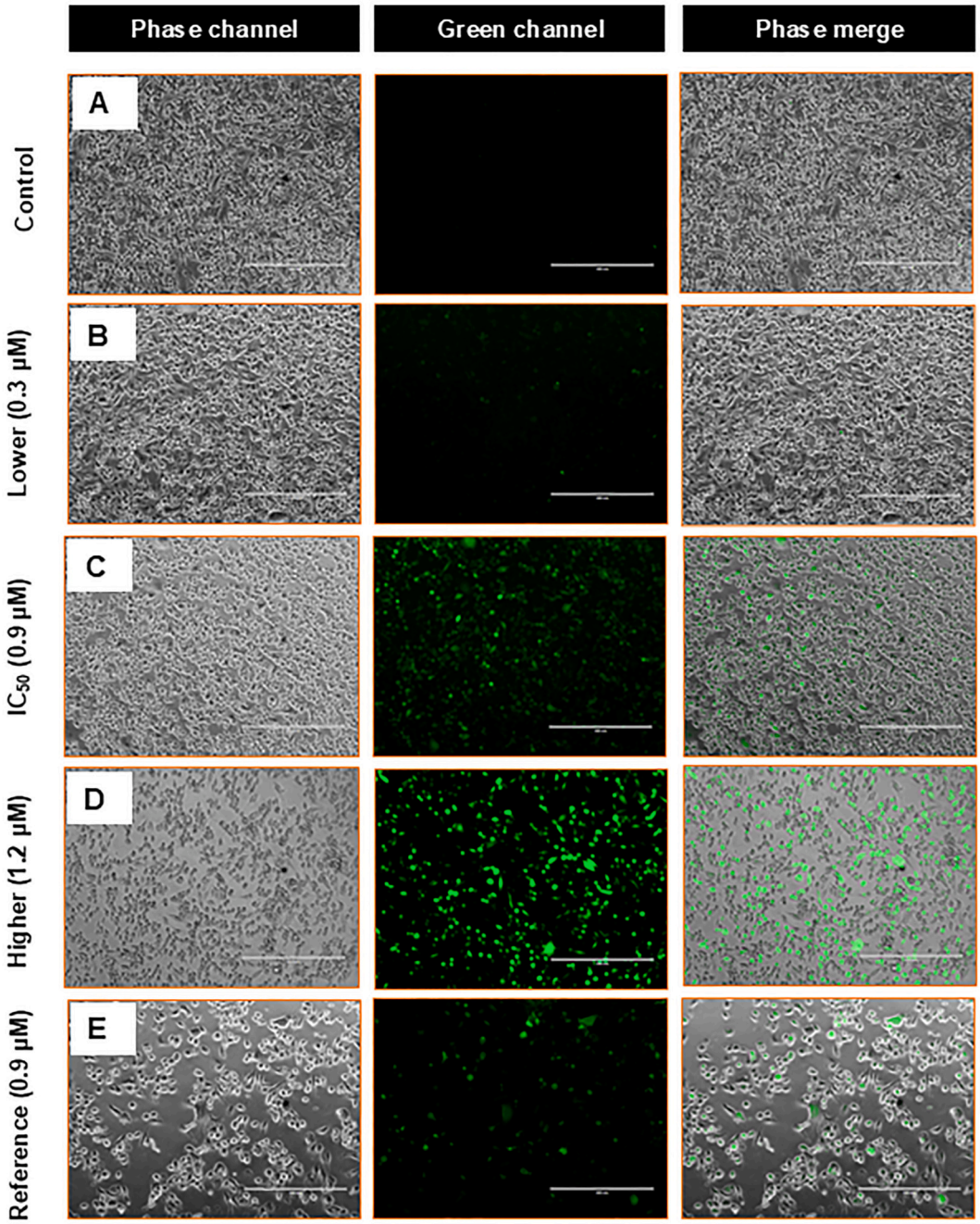

Fig. 4. Representative fluorescence microscopy images (Panels A-E) illustrate intracellular ROS generation in MDA-MB-231 cells after 24 h of treatment with various concentrations of test compound **2**. ROS levels were measured using the DCFH-DA fluorescent probe, which indicates oxidative stress within the cells. The images show a concentration-dependent increase in intracellular ROS, with Panel **A** representing the untreated control, Panel **B** showing cells treated with a low concentration (0.3 μM), Panel **C** corresponding to the IC_{50} concentration (0.9 μM), and Panel **D** showing cells treated with a higher concentration (1.2 μM). Panel **E** includes the pro-ligand $H'HL^{4\text{-}F}$ used as a reference compound for comparison. Scale bar: 400 μM; magnification: 100×.

concentrations leading to progressive chromatin condensation and membrane disruption.

The results suggest that compound **2** induces apoptosis in MDA-MB-231 cells, likely by interfering with DNA replication and transcription processes [91].

3.3.3. *In vitro generation of reactive oxygen species (ROS)*

Reactive oxygen species (ROS) support normal cell functions but also contribute to diseases like cancer. In cancer cells, controlled ROS levels are vital for processes like growth, differentiation, movement, and cell death. Monitoring ROS-antioxidant balance is key to understanding tumor development [92]. In vitro studies on MDA-MB-231 cells suggest that ROS generation may be linked to organotin(IV)-induced apoptosis [54,93].

The assay was performed on the most active test compound, **2**, to assess its impact on ROS production in MDA-MB-231 cells. Intracellular ROS levels were measured using the oxidation-sensitive fluorescent dye DCFH-DA [94]. Cells were exposed to compound **2** at concentrations around its IC_{50}: a lower dose (0.3 μM), the IC_{50} (0.9 μM), and a higher dose (1.2 μM), for 24 h. For comparison, cells were also treated with the pro-ligand $H'HL^{4\text{-}F}$ at 0.9 μM as a reference compound. Treatment with compound **2** at concentrations of 0.9 μM and 1.2 μM resulted in a marked increase in ROS production, as indicated by a strong green fluorescence signal (Fig. 4). In contrast, the lower concentration of 0.3 μM did not elicit a significant ROS response. Meanwhile, cells treated with $H'HL^{4\text{-}F}$ at 0.9 μM showed only a slight increase in ROS levels. These findings indicate that compound **2**, unlike $H'HL^{4\text{-}F}$, significantly increases ROS generation in a concentration-dependent manner, underscoring its potential involvement in modulating oxidative stress pathways in MDA-MB-231 cells.

3.3.4. *Analysis of mitochondrial distribution patterns*

The impact of tin compound **2** on mitochondrial morphology and subcellular distribution in MDA-MB-231 cells was evaluated using MitoTracker Red and Hoechst staining. MitoTracker Red, a fluorescent dye, was employed to visualize mitochondrial distribution within the cytoplasm, while Hoechst stain was used to label the nuclei, providing a contrasting reference. In untreated cells, MitoTracker Red fluorescence intensity was consistently high, suggesting a strong mitochondrial membrane potential. Mitochondria were primarily concentrated in the perinuclear region, extending radially toward the cell periphery, which aligns with their function in supporting cellular energy needs. In contrast, cells treated with compound **2** led to clear disruptions in the normal shape and organization of mitochondria. At a lower

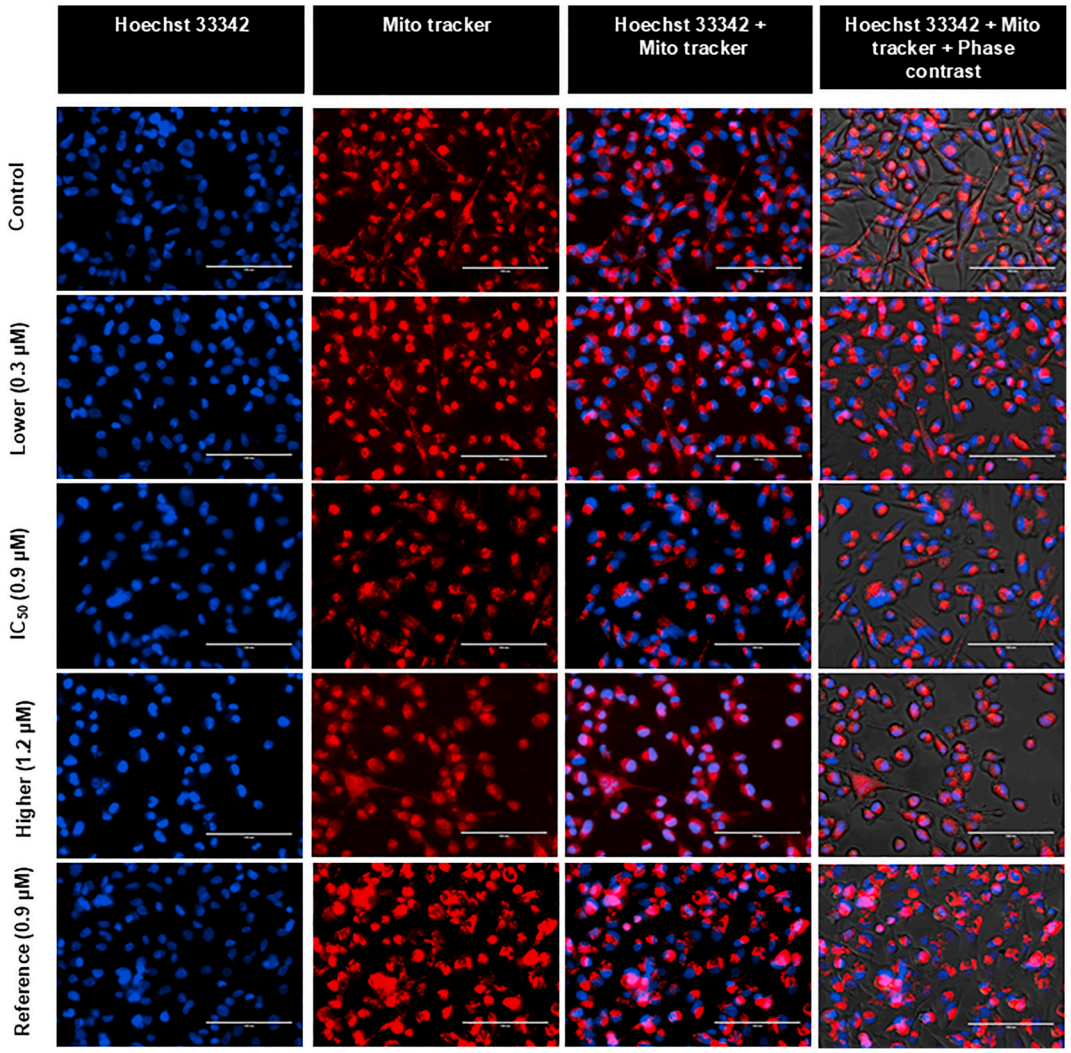

Fig. 5. Representative images illustrate mitochondrial morphology and subcellular distributions in MDA-MB-231 cells stained with MitoTracker Red and Hoechst 33342, following 24 h treatment with varying concentrations of test compound **2**. The pro-ligand $H'HL^{4\text{-}F}$ was included as reference. After treatment, cells were incubated with the fluorescent dyes at 37 °C for 30 min to visualize mitochondrial distribution. Imaging was performed using a fluorescence microscope. Scale bar: 100 μM; magnification: 400×. (For interpretation of the references to colour in this figure legend, the reader is referred to the web version of this article.)

concentration (0.3 μM), mitochondrial aggregation was observed, indicated by a bright red signal surrounding the nucleus. This aggregation became increasingly pronounced at higher concentrations of 0.9 μM and 1.2 μM (Fig. 5). Closer examination showed that the mitochondria had broken into smaller, dot-like pieces, spots or depressions, a typical sign of mitochondrial fission. Subcellular redistribution of mitochondria was also evident, with pronounced perinuclear clustering in treated cells compared to the controls. On the other hand, the cells treated with reference compound H'HL$^{4\text{-F}}$ (0.9 μM) resulted in only limited mitochondrial aggregation, indicating a comparatively lower level of bioactivity under the tested conditions. The findings show that compound **2** induces mitochondrial fragmentation, membrane depolarization, and perinuclear clustering in MDA-MB-231 cells, disrupting mitochondrial dynamics and bioenergetic function, which may contribute to its antiproliferative or pro-apoptotic effects.

3.3.5. *Detection of mitochondrial membrane potential (MMP)*

To evaluate the effect of the compound **2** and the reference compound H'HL$^{4\text{-F}}$ on mitochondrial membrane potential (ΔΨm) in MDA-MB-231 triple-negative breast cancer cells, the fluorescent dye JC-1 was employed. JC-1 accumulates in mitochondria in a membrane potential-dependent manner. In mitochondria with an intact membrane potential (ΔΨm), JC-1 forms red fluorescent aggregates (J-aggregates), whereas in depolarized mitochondria, it remains in its green-fluorescent monomeric form. The results showed that untreated MDA-MB-231 cells displayed strong red fluorescence localized to the mitochondria, indicating a well-maintained ΔΨm. In contrast, treatment with compound **2** resulted in a dose-dependent reduction in mitochondrial membrane potential (ΔΨm). As the concentration of compound **2** increased from 0.3 μM to 1.2 μM, a corresponding increase in green fluorescence was detected, indicating progressive mitochondrial depolarization (Fig. 6). At the IC_{50} concentration (0.9 μM) and above (1.2 μM), cells exhibited a marked reduction in red J-aggregate fluorescence alongside a significant rise in green monomeric fluorescence, confirming the loss of ΔΨm. In contrast, cells treated with the reference compound H'HL$^{4\text{-F}}$ exhibited predominantly red fluorescence with minimal green fluorescence,

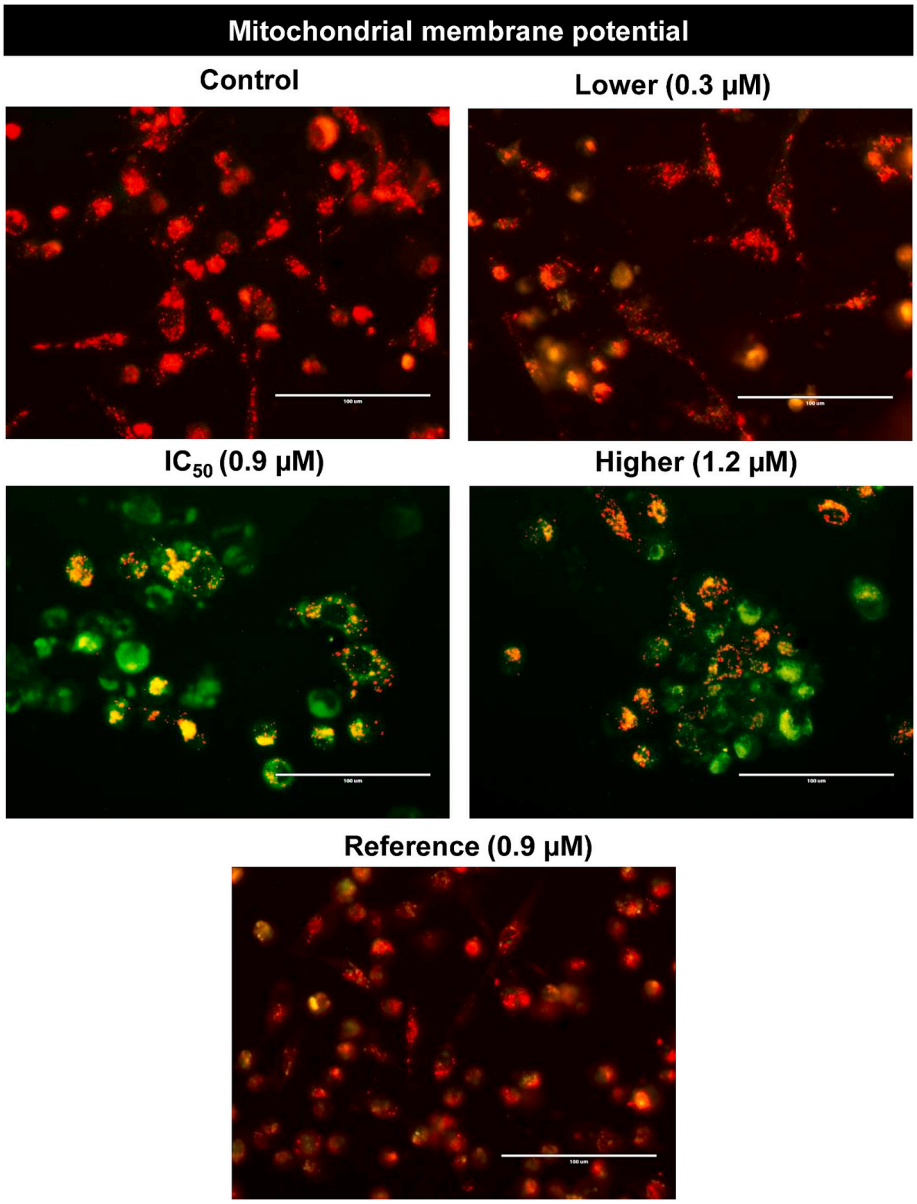

Fig. 6. Representative images illustrate mitochondrial membrane potential in MDA-MB-231 cells stained with JC-1, following 24 h treatment with varying concentrations of test compound **2**. The pro-ligand H'HL$^{4\text{-F}}$ was included as reference. After treatment, cells were incubated with the fluorescent dyes at 37 °C for 30 min to visualize mitochondrial membrane potential (ΔΨm). Imaging was performed using a fluorescence microscope. Scale bar: 100 μM; magnification: 400×.

indicating that H'HL$^{4\text{-F}}$ had little to no effect on mitochondrial membrane potential. These results emphasize that compound **2**, causes a pronounced, dose-dependent disruption of ΔΨm, highlighting its strong impact on mitochondrial function in MDA-MB-231 cells.

3.3.6. *Cell cycle analysis*

Flow cytometric analysis of propidium iodide (PI)-stained MDA-MB-231 cells revealed notable alterations in cell cycle progression following treatment with compound **2** and the reference compound H'HL$^{4\text{-F}}$. The results demonstrated a concentration-dependent increase in cell accumulation at the G0/G1 phase, indicating cell cycle arrest at this checkpoint. At the lower concentration of 0.3 μM, both compounds exhibited minimal effects compared to the untreated control. However, at the IC_{50} concentration (0.9 μM) and a higher dose (1.2 μM), compound **2** induced a pronounced G0/G1 phase arrest, with 74.83 % and 78.43 % of cells accumulating in this phase, respectively (Fig. 7). This arrest was accompanied by a corresponding reduction in the S-phase population to 8.26 % and 10.83 %, suggesting a dose-dependent suppression of DNA synthesis. In contrast, H'HL$^{4\text{-F}}$ caused only modest changes in cell cycle distribution, even at elevated concentrations. It is worth mentioning that a minor sub-G1 population was detected but excluded from the cell cycle graph in order to focus on functional cell cycle arrest in viable cells. Cell cycle arrest in the G0/G1 phase represents a critical anti-proliferative mechanism, as it prevents cancer cells from progressing into the DNA synthesis (S) phase, thereby inhibiting uncontrolled proliferation, a hallmark of malignancy. These findings highlight the superior efficacy of compound **2** in inducing G0/G1 arrest, underscoring its potential as a more potent modulator of cell cycle progression in MDA-MB-231 cells.

Among the triorganotin(IV) derivatives of Schiff bases containing azomethine and diazenyl functional groups shown in Scheme 1, the ligand scaffold of tri-*n*-butyltin complexes with structural type **V** (X = CO_2Me) closely resembles [*n*-$Bu_3Sn(HL^{4\text{-F}})$] (compound **2**), studied herein, differing only by the substitution of a fluorine atom with a carbomethoxy (CO_2Me) group. Moreover, [*n*-$Bu_3Sn(HL^{4\text{-CO2Me}})$] has been evaluated for its cytotoxic activity against a panel of seven human tumor cell lines [53]. This compound exhibited cytotoxicity values of 267, 126, 260, 261, 238, 165, and 149 μM against the A498 (renal), EVSA-T (ER-/PgR- breast), H226 (non-small-cell lung), IGROV (ovarian), M19 MEL (melanoma), MCF-7 (ER+/PgR+ breast), and WIDR (colon) cancer cell lines, respectively. In contrast, compound **2** demonstrated a markedly enhanced cytotoxic effect, with an IC_{50} value of 0.90 ± 0.05 μM against MDA-MB-231 breast cancer cells. While a direct comparison is limited due to the use of different cell lines, the data nonetheless underscore the potent cytotoxicity of compound **2**.

4. Conclusions

In this study, five novel tri-*n*-butyltin based compounds were synthesized by integrating anticancer pharmacophores from a variety of chemical scaffolds, including tri-*n*-butyltin moieties, azomethine and diazenyl functional groups, and fluorinated substituents. The resulting compounds [*n*-$Bu_3Sn(HL^{H})$] (**1**), [*n*-$Bu_3Sn(HL^{4\text{-F}})$] (**2**), [*n*-$Bu_3Sn(HL^{2\text{-}}$

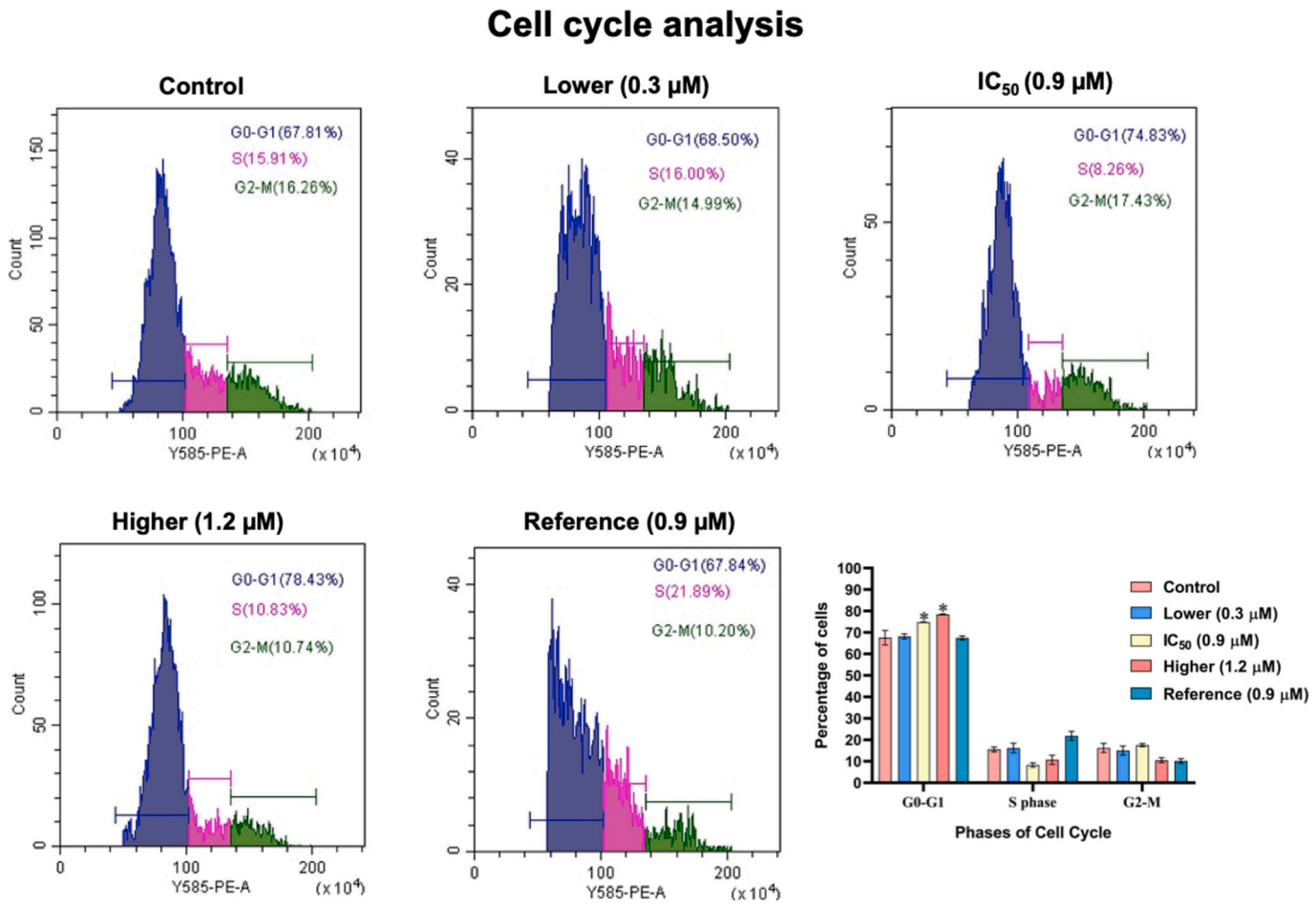

Fig. 7. Flow cytometric analysis of cell cycle distribution in untreated (control) and compound-treated MDA-MB-231 cells, stained with propidium iodide (PI). Cells were treated with varying concentrations of compound **2** and H'HL$^{4\text{-F}}$. Treatment resulted in a significant G0/G1-phase arrest, as indicated by an increased proportion of cells in this phase compared to controls. Percentages of cells in the G1, S, and G2/M phases are shown, with statistical significance (*$p < 0.05$) determined by using One-way ANOVA followed by Tukey's post hoc test.

^{CF3})] (**3**), [*n*-$Bu_3Sn(HL^{3\text{-}CF3})$] (**4**) and [*n*-$Bu_3Sn(HL^{4\text{-}CF3})$] (**5**) were synthesized and thoroughly characterized using FT-IR (ATR) spectroscopy and multinuclear NMR spectroscopy (^{1}H, ^{13}C, and ^{119}Sn). Single-crystal X-ray analysis revealed that compounds **2**, **4**, and **5** form mono-periodic chains structures in the solid state, which dissociate into discrete four-coordinate species in solution, as confirmed by ^{119}Sn NMR spectroscopy.

The anticancer potential of these compounds was investigated in the context of experimental oncology, with a particular focus on triple-negative breast cancer (TNBC) MDA-MB-231 cells. *In vitro* anti-proliferative assays revealed that compounds **1**–**5** exhibited significant cytotoxicity against MDA-MB-231 cells, with IC_{50} values ranging from 0.90 to 2.18 μM. Notably, the fluorinated complex [*n*-$Bu_3Sn(HL^{4\text{-}F})$] (compound **2**) demonstrated the highest cytotoxicity, with an IC_{50} of 0.90 ± 0.05 μM, while showing minimal toxicity toward normal HEK cells (IC_{50} = 33.8 ± 0.26. Compound **2** exhibited a dose-dependent cytotoxic effect and showed superior efficacy in inducing G0/G1 cell cycle arrest, underscoring its potential as a promising modulator of cell cycle progression in TNBC cells. Among the compounds, the fluoro-substituted derivative [*n*-$Bu_3Sn(HL^{4\text{-}F})$] **2** holds potential for synthesizing a variety of fluoro-substituted triorganotin(IV) derivatives.

CRediT authorship contribution statement

Tushar S. Basu Baul: Writing – review & editing, Writing – original draft, Supervision, Resources, Project administration, Investigation, Conceptualization. **Amon Das:** Software, Methodology, Investigation, Data curation. **Avishek Khatiwara:** Validation, Software, Methodology, Investigation, Data curation. **Vivek Kumar Sharma:** Validation, Software, Methodology, Investigation, Data curation. **Andrew Duthie:** Writing – review & editing, Formal analysis, Data curation. **Biplob Koch:** Supervision, Resources, Project administration, Investigation. **Sean Parkin:** Writing – review & editing, Validation, Software, Resources.

Declaration of competing interest

The authors declare no conflict of interest.

Acknowledgements

AD and AK thank University Grants Commission, New Delhi for the award of non-NET fellowships. Authors (TSBB, AD and AK) thank SAIF-NEHU, Shillong for providing NMR measurements and the DST-FIST program (No. SR/FST/CS-II/2019/99(C)), Government of India, for providing the HRMS instrument to the Department of Chemistry, NEHU, Shillong. Deakin University's Advanced Characterization Facility is acknowledged for use of the NMR instrumentation. SP thanks the US NSF MRI program (grant CHE-1625732). BK acknowledges Banaras Hindu University for providing funding under the IoE scheme (File No. R/Dev/D/IoE/Incentive/2021-22/32449).

Appendix A. Supplementary data

Supplementary data to this article can be found online at https://doi.org/10.1016/j.jinorgbio.2025.113013.

Data availability

ESI contains all the data

References

[1] A.G. Davies, M. Gielen, K.H. Pannell, E.R.T. Tiekink, Tin Chemistry – Fundamentals, Frontiers and Applications, John Wiley & Sons Ltd, Chichester, England, 2008.
[2] C.G. dos Santos, G.M. de Lima, Tin and organotin coordination polymers and covalently bonded supramolecular materials – the last 15 years of research, Coord. Chem. Rev. 410 (2020) 213236.
[3] R. Joshi, N. Tomar, S. Pokharia, I. Joshi, Recent advancements in organotin(IV) complexes of drugs: synthesis, characterization, and application, Results Chem. 5 (2023) 100955.
[4] B.Z. Momeni, A. Abd-El-Aziz, N. Ma, A.S. Abd-El-Aziz, Organotin(IV) from simple complexes to macromolecules: a review inspired by the late professor Charles Carraher, J. Inorg. Organomet. Polym. Mater. 34 (2024) 2855–2892.
[5] S.K. Hadjikakou, N. Hadjiliadis, Antiproliferative and anti-tumor activity of organotin compounds, Coord. Chem. Rev. 253 (2009) 235–249.
[6] A. Alama, B. Tasso, F. Novelli, F. Sparatore, Organometallic compounds in oncology: implications of novel organotins as antitumor agents, Drug Discov. Today 14 (2009) 500–508.
[7] C.N. Banti, S.K. Hadjikakou, T. Sismanoglu, N. Hadjiliadis, Anti-proliferative and antitumor activity of organotin(IV) compounds. An overview of the last decade and future perspectives, J. Inorg. Biochem. 194 (2019) 114–152.
[8] A. Paul, S. Hazra, M.F.C. Guedes da Silva, A.J.L. Pombeiro, Biological evaluation of azo- and imino-based carboxylate triphenyltin(IV) compounds, Eur. J. Inorg. Chem. 2020 (2020) 930–941.
[9] S.N.S. Annuar, N.F. Kamaludin, N. Awang, K.M. Chan, Cellular basis of organotin (IV) derivatives as anticancer metallodrugs: a review, Front. Chem. 9 (2021) 657599.
[10] S. Hadi, E.K. Winarno, H. Winarno, K.N. Berawi, T. Suhartati, N. Noviany, W. Simanjuntak, Y. Yandri, Synthesis and *in vitro* activity investigation of some dibutyl-, diphenyl- and triphenyltin(IV) carboxylates against leukemia cancer cell, L-1210, Pure Appl. Chem. 95 (2023) 823–832.
[11] S. Hussain, S. Shujah, A. Rehman, S.T. Hussain, M. Hussain, I. Naz, A. Alhodaib, Synthesis, spectroscopic characterization, antileishmanial, DNA binding, antioxidant, cytotoxicity, antifungal and antibacterial studies of organotin(IV) carboxylate complexes, Arab. J. Chem. 16 (2023) 105306.
[12] S. Rahim, A. Sadiq, A. Javed, M. Kubicki, B. Kariuki, M. Assad, N. Muhammad, N. Fatima, M. Khan, A.F. Al-Asmari, F. Al-Asmari, *In vitro* anticancer, antioxidant, antimicrobial, antileishmanial, enzymes inhibition and *in vivo* anti-inflammatory activities of organotin(IV) derivatives of 4-bromophenoxyacetic acid, J. Mol. Struct. 1313 (2024) 138703.
[13] M. Sirajuddin, S. Ali, M. Tariq, H. Khan, A. Alobaid, A. Bari, Synthesis, characterization, exploration of anti-cancer, anti-leishmanial, anti-microbial activities, pharmacokinetic and docking studies of Sn(IV) complexes, Inorg. Chim. Acta 568 (2024) 122082.
[14] M. Shamsi, W.M. Al-Asbahy, H.Q.N. Al-Areqi, F.A.M. Alzowahi, Probing the biomolecular interactions of DNA/HSA with the new Sn(IV) complex and computational perspectives: design, synthesis, characterization, anticancer activity, and molecular modelling approach, J. Med. Chem. 67 (2024) 21841–21858.
[15] T.A. Antonenko, Y.A. Gracheva, D.B. Shpakovsky, M.A. Vorobyev, D.M. Mazur, V. A. Tafeenko, Y.F. Oprunenko, E.F. Shevtsova, P.N. Shevtsov, A.A. Nazarov, E. R. Milaeva, Biological activity of novel organotin compounds with a Schiff base containing an antioxidant fragment, Int. J. Mol. Sci. 24 (2023) 2024.
[16] W. Jiang, Q. Luo, W. Huang, Y. Tan, Y. Peng, Synthesis, anticancer activity, and mechanistic investigations of aryl-alkyl diorganotin arylformylhydrazone complexes, J. Inorg. Biochem. 262 (2025) 112756.
[17] S. Sharma, V. Kaur, P. Duhan, R. Singh, N. Agnihotri, Evaluation of anticancer activity of novel and tumor-targeted glutamine-conjugated organotin(IV) compounds in colorectal cancer – an *in vitro* and *in vivo* study, J. Med. Chem. 68 (2025) 2593–2607.
[18] X. Wu, L. Wu, Z. Li, W. Tian, T. Li, Synthesis, crystal structure, and anticancer activity of organotin(IV) complexes based on chlorine substituted aryl ligands, Med. Chem. Res. 34 (2025) 855–869.
[19] Y. Tan, Z. Zhang, J. Liu, Y. Tan, W. Jiang, Syntheses, crystal structures, and anticancer activities of organotin carboxylates based on Alrestatin, J. Mol. Struct. 1322 (2025) 140697.
[20] E. Nikitin, S. Fedorov, Y. Gracheva, K. Lyssenko, A. Semykin, Y. Oprunenko, N. Sobolev, D. Mazur, L. Dubova, E. Shevtsova, E. Milaeva, Organotin carboxylates with bulky substituents. Synthesis, structure, cytotoxicity and antioxidant activity, Inorg. Chim. Acta 574 (2025) 122388.
[21] V. Singh, R. Singh, P. Goswami, P.P. Manna, T.S. Basu Baul, A. Mandal, A.K. Singh, B. Koch, Influences of aqua-(2-formylbenzoato) triphenyltin(IV) on regression of hypoxic solid tumor through mitochondrial mediated pathway by inhibiting Hif-1 alpha, Sci. Rep. 15 (2025) 5302.
[22] R.R. Arraq, A.G. Hadi, Synthesis, identification, and anti-oxidant activity of di-organotin(IV)-cephalexin complexes, J. Med. Chem. Sci. 6 (2023) 392–401.
[23] D.K. Kovala-Demertzi, V. Dokorou, Z. Ciunik, N. Kourkoumelis, M.A. Demertzis, Organotin mefenamic complexes-preparations, spectroscopic studies and crystal structure of a triphenyltin ester of mefenamic acid: novel anti-tuberculosis agents, Appl. Organomet. Chem. 16 (2002) 360–368.
[24] H. Iqbal, S. Ali, S. Shahzadi, Antituberculosis study of organotin(IV) complexes: a review, Cogent Chem. 1 (2015) 1029039.
[25] T.S. Basu Baul, Antimicrobial activity of organotin(IV) compounds: a review, Appl. Organomet. Chem. 22 (2008) 195–204.
[26] M. Kumar, Z. Abbas, H.S. Tuli, A. Rani, Organotin complexes with promising therapeutic potential, Curr. Pharmacol. Rep. 6 (2020) 167–181.
[27] S. Hadi, B. Irawan, T. Yandri, Synthesis, characterization and the antifungal activity test of some organotin(IV) benzoates, J. Phys. Conf. Ser. 1751 (2021) 012099.

[28] C. Hansch, R.P. Verma, Larvicidal activities of some organotin compounds on mosquito larvae: a QSAR study, Eur. J. Med. Chem. 44 (2009) 260–273.

[29] S. Hadi, M. Noviany, Rilyanti, *in vitro* antimalarial activity of some organotin(IV) 2-nitrobenzoate compounds against plasmodium falciparum, Maced. J. Chem. Chem. Eng. 37 (2018) 185–191.

[30] S. Hadi, M.D. Fenska, N. Noviany, H. Satria, W. Simanjuntak, M.M. Naseer, Synthesis and antimalarial activity of some triphenyltin(IV) aminobenzoate compounds against plasmodium falciparum, Main Group Met. Chem. 44 (2021) 256–260.

[31] J. Otera, Transesterification, Chem. Rev. 93 (1993) 1449–1470.

[32] P. Espinet, A.M. Echavarren, The mechanisms of the stille reaction, Angew. Chem. Int. Ed. 43 (2004) 4704–4734.

[33] a) S.R. Sanapureddy, L. Plasseraud, (n-Bu_2Sn)$_2$O(CO_3): An active, robust and recyclable organotin(IV) for the direct synthesis of linear organic carbonates from carbon dioxide and alcohols, Appl. Organomet. Chem. 31 (2017) e3807;
b) S. Wang, C. Chen, P. Yang, Y. Guo, B. Wang, H. Niu, Q. Zhang, J. Wang, Facile one-pot preparation of organotin-oxometalate polymers for efficient synthesis of dimethyl carbonate from CO_2, Ind. Chem. Res. 63 (2024) 10151–10161.

[34] a) A.M. Cantón-Díaz, B.M. Muñoz-Flores, I. Moggio, E. Arias, A. De León, M. C. García-López, R. Santillan, M.E. Ochoa, V.M. Jiménez-Pérez, One-pot microwave-assisted synthesis of organotin Schiff bases: an optical and electrochemical study towards their effects in organic solar cells, New J. Chem. 42 (2018) 14586–14596;
b) E. Geringer, M. Gerhard, S. Dehnen, Introducing distinct structural and optical properties into organotin sulfide clusters by the attachment of perylenyl and corannulenyl groups, Inorg. Chem. 60 (2021) 19381–19392.

[35] a) C.C. Jiménez, A. Enríquez-Cabrera, O. González-Antonio, J. Ordoñez-Hernández, P.G. Lacroix, P. Labra-Vázquez, N. Farfán, R. Santillan, State of the art of boron and tin complexes in second- and third-order nonlinear optics, Inorganics 6 (2018) 131;
b) F. Ziese, J. Wang, I. Rojas León, S. Dehnen, S. Sanna, Origin of the nonlinear optical response in organotetrel, molecules, (hetero)adamantane-type clusters with organic substituents, and related species, J. Phys. Chem. A 128 (2024) 8360–8372.

[36] A.F. Akbulatov, A.Y. Akyeva, P.G. Shangin, N.A. Emelianov, I.V. Krylova, M. O. Markova, L.D. Labutskaya, A.V. Mumyatov, E.I. Tuzharov, D.A. Bunin, L. A. Frolova, M.P. Egorov, M.A. Syroeshkin, P.A. Troshin, Sn and Ge complexes with redox-active ligands as efficient interfacial membrane-like buffer layers for p-i-n perovskite solar cells, Membranes 13 (2023) 439.

[37] a) A. Torres-Huerta, B. Rodríguez-Molina, H. Höpfl, M.A. Garcia-Garibay, Synthesis and solid-state characterization of self-assembled macrocyclic molecular rotors of bis(dithiocarbamate) ligands with diorganotin(IV), Organometallics 33 (2014) 354–362;
b) A.M. Cantón-Díaz, B.M. Muñoz-Flores, L.F. Macías-Gamboa, I. Moggio, E. Arias, H.V. Rasika Días, G. Colombo, S. Brenna, V. Jiménez-Pérez, Temperature-dependent photoluminescence down to 77 K of organotin molecular rotors: eco-friendly synthesis, photophysical characterization, X-ray structures, and DFT studies, Dalton Trans. 53 (2024) 15010–15031.

[38] a) A.Y. Castrejón-Antúnez, M. Mendoza-Mendoza, D.I. Olea-López, F. Medrano, H. Tlahuext, J. Guerrero-Álvarez, G. Vargas-Pineda, C. Godoy-Alcántar, Chlorodiphenyltin(IV) dithiocarbamate complexes as chemodosimeters and host for anions and neutral compounds in solution, Polyhedron 111 (2016) 132–142;
b) N.A. Rodríguez-Uribe, M.Á. Claudio-Catalán, F. Medrano, G. Pina-Luis, H. Tlahuext, C. Godoy-Alcántar, Anion interaction with homoditopic chlorodiorganotin(IV) dithiocarbamate complexes derived from a naphthalene diimide. A pathway to obtain metallomacrocycles, Polyhedron 186 (2020) 114615;
c) M.M. Naseer, K. Jurkschat, Organotin-based receptors for anions and ion pairs, Chem. Commun. 53 (2017) 8122–8135;
d) V. Arens, M.M. Naseer, M. Lutter, L. Iovkova-Behrens, K. Jurkschat, Organotin-functionalized crown ethers as ditopic hosts for lithium salts: synthesis, structures and complexation studies of X_3SnCH_2[16]-crown-5 (X = I, Br, cl), Eur. J. Inorg. Chem. 2018 (2018) 1540–1545;
e) N. Alashkar, M. Arca, H. Alnasr, M. Lutter, V. Lippolis, K. Jurkschat, Water-soluble organotin compounds – syntheses, structures and reactivity towards fluoride anions in water, Eur. J. Inorg. Chem. 2020 (2020) 3925–3936.

[39] T.S. Basu Baul, A. Chaurasiya, M. Rabha, S. Khatua, A. Lyčka, D. Schollmeyer, K. Jurkschat, Diorganotin compounds containing α-aminoacidato Schiff base ligands derived from functionalized 2-hydroxy-5-(aryldiazenyl)benzaldehyde. Syntheses, structures and sensing of hydrogen sulfide, Eur. J. Inorg. Chem. 2020 (2020) 1803–1813.

[40] T.S. Basu Baul, C. Masharing, G. Ruisi, R. Jirásko, M. Holčapek, D. de Vos, D. Wolstenholme, A. Linden, Self-assembly of extended Schiff base amino acetate skeletons, 2-{[(2*Z*)-(3-hydroxy-1-methyl-2-butenylidene)]amino} phenylpropionate and 2-{[(*E*)-1-(2-hydroxyaryl)alkylidene]amino} phenylpropionate skeletons incorporating organotin(IV) moieties: synthesis, spectroscopic characterization, crystal structures, and *in vitro* cytotoxic activity, J. Organomet. Chem. 692 (2007) 4849–4862.

[41] T.S. Basu Baul, S. Basu, D. de Vos, A. Linden, Amino acetate functionalized Schiff base organotin(IV) complexes as anticancer drugs: synthesis, structural characterization, and *in vitro* cytotoxicity studies, Investig. New Drugs 27 (2009) 419–431.

[42] T.S. Basu Baul, A. Paul, L. Pellerito, M. Scopelliti, C. Pellerito, P. Singh, P. Verma, A. Duthie, D. de Vos, R.P. Verma, U. Englert, Molecular basis of the interaction of novel tributyltin(IV) 2/4-[(*E*)-2-(aryl)-1-diazenyl]benzoates endowed with an improved cytotoxic profile: synthesis, structure, biological efficacy and QSAR studies, J. Inorg. Biochem. 104 (2010) 950–966.

[43] T.S. Basu Baul, A. Paul, L. Pellerito, M. Scopelliti, P. Singh, P. Verma, D. de Vos, Triphenyltin(IV) 2-[(*E*)-2-(aryl)-1-diazenyl]benzoates as anticancer drugs: synthesis, structural characterization, *in vitro* cytotoxicity and study of its influence towards the mechanistic role of some key enzymes, Investig. New Drugs 28 (2010) 587–599.

[44] T.S. Basu Baul, A. Paul, L. Pellerito, M. Scopelliti, A. Duthie, D. de Vos, R.P. Verma, U. Englert, An *in vitro* comparative assessment with a series of new triphenyltin(IV) 2−/4-[(*E*)-2-(aryl)-1-diazenyl]benzoates endowed with anticancer activities: structural modifications, analysis of efficacy and cytotoxicity involving human tumour cell lines, J. Inorg. Biochem. 107 (2012) 119–128.

[45] T.S. Basu Baul, D. Dutta, D. de Vos, H. Höpfl, P. Singh, Advancement towards tin-based anticancer chemotherapeutics: structural modification and computer modeling approach to drug-enzyme interactions, Curr. Med. Chem. 12 (2012) 2810–2826.

[46] T.S. Basu Baul, D. Dutta, B.G.M. Rocha, M.F.C. Guedes da Silva, A. Lyčka, Triorganostannyl(IV) benzoates with pendulous framework appended with ferrocene scaffold, J. Organomet. Chem. 882 (2019) 33–41.

[47] T.S. Basu Baul, K.S. Singh, A. Linden, X. Song, G. Eng, Synthesis, spectroscopic characterization of tribenzyltin(IV) complexes of polyaromatic carboxylic acid ligands: crystal and molecular structures of $Bz_3Sn[O_2CC_6H_4\{N{=}N(C_6H_3\text{-}4\text{-}OH(C(H){=}NC_6H_4X\text{-}4)\})\text{-}o](OH_2)$ (X = -cl, -OCH_3), Polyhedron 25 (2006) 3441–3448.

[48] T.S. Basu Baul, K.S. Singh, M. Holčapek, R. Jirásko, E. Rivarola, A. Linden, Synthesis, characterization and crystal structures of polymeric and dimeric triphenyltin(IV) complexes of 4-[((*E*)-1-{2-hydroxy-5-[(*E*)-2-(2-carboxyphenyl)-1-diazenyl]phenyl}methylidene)-amino]aryls, J. Organomet. Chem. 690 (2005) 4232–4242.

[49] K.S. Singh, M. Roy, S. Roy, B. Ghosh, N.M. Devi, C.B. Singh, L.K. Mun, Synthesis, characterization and antimicrobial activities of triorganotin(IV) complexes with azomethine carboxylate ligands: crystal structure of a tributyltin(IV) and a trimethyltin(IV) complex, J. Coord. Chem. 70 (2017) 361–380.

[50] T.S. Basu Baul, K.S. Singh, X. Song, A. Zapata, G. Eng, A. Lyčka, A. Linden, Synthesis and characterization of tributyltin(IV) complexes of 2-[(*E*)-2-(3-formyl-4-hydroxyphenyl)-1-diazenyl]benzoic acid and 4-[((*E*)-1-{2-hydroxy-5-[(*E*)-2-(2-carboxyphenyl)-1-diazenyl]phenyl}methylidene)amino]aryls – crystal structures of polymeric $(Bu_3Sn[O_2CC_6H_4\{N{=}N(C_6H_3\text{-}4\text{-}OH\text{-}5\text{-}CHO)\}\text{-}o])_n$ and $(Bu_3Sn[O_2CC_6H_4\{N{=}N(C_6H_3\text{-}4\text{-}OH(C(H){=}NC_6H_4Cl\text{-}4)\})\text{-}o])_n$ – toxicity studies on the second instar of Aedes aegypti mosquito larvae, J. Organomet. Chem. 689 (2004) 4702–4711.

[51] T.S. Basu Baul, K.S. Singh, M. Holčapek, R. Jirásko, A. Linden, X. Song, A. Zapata, G. Eng, Electrospray ionization mass spectrometry of tributyltin(IV) complexes and their larvicidal activity on mosquito larvae: crystal and molecular structure of polymeric $(Bu_3Sn[O_2CC_6H_4\{N{=}N(C_6H_3\text{-}4\text{-}OH(C(H){=}NC_6H_4OCH_3\text{-}4)\})\text{-}o])_n$, Appl. Organomet. Chem. 19 (2005) 935–944.

[52] A. Linden, T.S. Basu Baul, K.S. Singh, Catena-poly[[tri-n-butyltin(IV)]-μ-2-{(*E*)-4-hydroxy-3-[(*E*)-4-methylphenyliminomethyl]phenyldiazenyl}benzoato-κ^2O:O'], Acta Crystallogr. E61 (2005) m2711–m2713.

[53] T.S. Basu Baul, B. Hlychho, M.R. Addepalli, S. Kundu, D. de Vos, A. Linden, Synthesis and structures of polynuclear organotin(IV) complexes of a polyaromatic carboxylate ligand and cytotoxic evaluation in tumor cell lines, J. Organomet. Chem. 985 (2023) 122592.

[54] V. Singh, N.K. Rana, M. Kashif, P.P. Manna, T.S. Basu Baul, Aqua-(2-formylbenzoato)triphenyltin(IV) induces cell cycle arrest and apoptosis in hypoxic triple negative breast cancer cells, Toxicol. in Vitro 86 (2023) 105484.

[55] M. Singh, N.K. Rana, M.S. Muthu, A. Jha, T.S. Basu Baul, B. Koch, Enhanced *in vitro* therapeutic efficacy of triphenyltin(IV) loaded vitamin E TPGS against breast cancer therapy, Mater Today Commun 31 (2022) 103256.

[56] M. Singh, V. Singh, T.S. Basu Baul, B. Koch, TPGS loaded triphenyltin(IV) micelles induced apoptosis by upregulating p53 in breast cancer cells and inhibit tumor progression in T-cell lymphoma bearing mice, Life Sci. 308 (2022) 120937.

[57] N.Đ. Pantelić, B.B. Bojan Božić, N.R. Zmejkovski, B. Banjac, L.A. Dojčinović, G.N. Kaluđerović Wessjohann, *In vitro* evaluation of antiproliferative properties of novel organotin(IV) carboxylate compounds with propanoic acid derivatives on a panel of human cancer cell lines, Molecules 26 (2021) 3199.

[58] M. Sirajuddin, S. Ali, Organotin(IV) carboxylates as promising potential drug candidates in the field of cancer chemotherapy, Curr. Pharm. Des. 22 (2016) 6665–6681.

[59] P. Shah, A.D. Westwell, The role of fluorine in medicinal chemistry, J. Enzyme Inhib. Med. Chem. 22 (2007) 527–540.

[60] S. Purser, P.R. Moore, S. Swallow, V. Gouverneur, Fluorine in medicinal chemistry, Chem. Soc. Rev. 37 (2008) 320–330.

[61] A.S. Nair, A.K. Singh, A. Kumar, S. Kumar, S. Sukumaran, V.P. Koyiparambath, L. K. Pappachen, T.M. Rangarajan, H. Kim, B. Mathew, FDA-approved trifluoromethyl group-containing drugs: a review of 20 years, Processes 10 (2022) 2054.

[62] Y. Du, Y. Bian, D. Baecker, G. Dhawan, A. Semghouli, L. Kiss, W. Zhang, A. E. Sorochinsky, V.A. Soloshonok, J. Han, Fluorine in the pharmaceutical industry: FDA-approved fluorine-containing drugs in 2024, Chem. Eur. J. 31 (2025) e202500662.

[63] J.C. Páez-Franco, M.R. Zermeño-Ortega, C.M. de la O-Contreras, D. Canseco-González, J.R. Parra-Unda, A. Avila-Sorrosa, R.G. Enríquez, J.M. Germán-Acacio, D. Morales-Morales, Relevance of fluorinated ligands to the design of metallodrugs for their potential use in cancer treatment, Pharmaceutics 14 (2022) 402, https://doi.org/10.3390/pharmaceutics14020402.

[64] T.S. Basu Baul, A. Das, S. Das Pramanik, P. Roy, A. Duthie, S. Parkin, Structural dynamics and evaluation of anti-proliferative effects of di-*n*-butyltin and triphenyltin fluoroazosalicylates on DU-145 prostate cancer cells, J. Mol. Struct. 1325 (2025) 140973.

[65] T.S. Basu Baul, A. Das, R. Tamang, A. Duthie, B. Koch, S. Parkin, Synthesis, structural analysis, and systematic exploration of the antitumor activities of triphenyltin(IV) 2-hydroxy-5-(phenyldiazenyl)benzoates through the modulation of trifluoromethyl variants, J. Inorg. Biochem. 269 (2025) 112898.
[66] T.S. Basu Baul, S.P. Pyke, K.K. Sarma, E.R.T. Tiekink, Crystal and molecular structure of aquatriphenyltin 2-(3-formyl-4-hydroxyphenylazo)benzoate, Main Group Met. Chem. 19 (1996) 807–814.
[67] S. Parkin, H. Hope, Macromolecular cryocrystallography: cooling, mounting, storage and transportation of crystals, J. Appl. Crystallogr. 31 (1998) 945–953.
[68] Bruker-AXS, *APEX5*, *SMART*, *SAINT*, Bruker AXS Inc, Madison, Wisconsin, USA, 2023.
[69] L. Krause, R. Herbst-Irmer, G.M. Sheldrick, D. Stalke, Comparison of silver and molybdenum microfocus X-ray sources for single-crystal structure determination, J. Appl. Crystallogr. 48 (2015) 3–10.
[70] S. Parkin, B. Moezzi, H. Hope, *XABS2*: an empirical absorption correction program, J. Appl. Crystallogr. 28 (1995) 53–56.
[71] A.L. Spek, checkCIF validation ALERTS: what they mean and how to respond, Acta Crystallogr. E76 (2015) 1–11.
[72] S. Parkin, Expansion of scalar validation criteria to three dimensions: the R-tensor, Acta Crystallogr. A56 (2000) 157–162.
[73] G.M. Sheldrick, *SHELXT* – integrated space-group and crystal-structure determination, Acta Crystallogr. A71 (2015) 3–8.
[74] G.M. Sheldrick, Crystal structure refinement with SHELXL, Acta Crystallogr. C71 (2015) 3–8.
[75] S.R. Parkin, Practical hints and tips for solution of pseudo-merohedric twins: three case studies, Acta Crystallogr. E77 (2021) 452–465.
[76] M. Sevvana, M. Ruf, I. Usón, G.M. Sheldrick, R. Herbst-Irmer, Non-merohedral twinning: from minerals to proteins, Acta Crystallogr. D75 (2019) 1040–1050.
[77] T. Mosmann, Rapid colorimetric assay for cellular growth and survival: application to proliferation and cytotoxicity assays, J. Immunol. Methods 65 (1983) 55–63.
[78] K. Liu, P.C. Liu, R. Liu, X. Wu, Dual AO/EB staining to detect apoptosis in osteosarcoma cells compared with flow cytometry, Med. Sci. Monit. Basic Res. 21 (2015) 15–20.
[79] K. Neikirk, A.G. Marshall, B. Kula, N. Smith, S. LeBlanc, A. Hinton Jr., MitoTracker: a useful tool in need of better alternatives, Eur. J. Cell Biol. 102 (2023) 151371.
[80] A. Perelman, C. Wachtel, M. Cohen, S. Haupt, H. Shapiro, A. Tzur, JC-1: alternative excitation wavelengths facilitate mitochondrial membrane potential cytometry, Cell Death Dis. 3 (2012) e430, https://doi.org/10.1038/cddis.2012.171.
[81] a) P.N. Nelson, R.A. Taylor, Theories and experimental investigations of the structural and thermotropic mesomorphic phase behaviors of metal carboxylates, Appl. Petrochem. Res. 4 (2014) 253–285;
b) G.B. Deacon, R.J. Philips, Relationships between the carbon-oxygen stretching frequencies of carboxylato complexes and the type of carboxylate coordination, Coord. Chem. Rev. 33 (1980) 227–250.
[82] M.P. Kasalović, S. Jelača, D. Dimić, D. Maksimović-Ivanić, V.V. Jevtić, S. Mijatović, T. Rüffer, G.N. Kaluđerović, N.Đ. Pantelić, Organic moiety on Sn(IV) does matter for in vitro mode of action: nBu$_3$Sn(IV) compounds with carboxylato *N*-functionalized 2-quinolones induce anoikis-like cell death in A375 cells, Pharmaceutics 16 (2024) 1529, https://doi.org/10.3390/pharmaceutics16121529.
[83] M. Nádvorník, J. Holeček, K. Handlíř, A. Lyčka, The ^{13}C and ^{119}Sn NMR spectra of some four- and five-coordinate tri-*n*-butyltin(IV) compounds, J. Organomet. Chem. 275 (1984) 43–51.
[84] A. Lyčka, J. Holeček, M. Nádvorník, K. Handlíř, ^{13}C, ^{15}N and ^{119}Sn NMR spectral evidence for tin five-coordination in triorganotin(IV) oxinates, J. Organomet. Chem. 280 (1985) 323–329.
[85] R. Willem, I. Verbruggen, M. Gielen, M. Biesemans, B. Mahieu, T.S. Basu Baul, E.R. T. Tiekink, Correlating Mössbauer and solution-and solid-state ^{117}Sn NMR data with X-ray diffraction structural data of triorganotin 2-[(*E*)-2-(2-Hydroxy-5-methylphenyl)-1-diazenyl]benzoates, Organometallics 17 (1998) 5758–5766.
[86] S.R. Parkin, E.J. Behrman, Channel-forming solvate crystals and isostructural solvent-free powder of 5-hydroxy-6-methyl-2-pyridone, Acta Crystallogr. C67 (2011) o324–o328.
[87] A.L. Spek, PLATON SQUEEZE: a tool for the calculation of the disordered solvent contribution to the calculated structure factors, Acta Crystallogr. C71 (2015) 9–18.
[88] A.W. Addison, T.N. Rao, J. Reedijk, J.V. Rijn, G.C. Verschoor, Synthesis, structure, and spectroscopic properties of copper(II) compounds containing nitrogen-Sulphur donor ligands; the crystal and molecular structure of aqua[1,7-bis(*N*-methylbenzimidazol-2′-yl)-2,6-dithiaheptane]copper(II) perchlorate, J. Chem. Soc. Dalton Trans. 7 (1984) 1349–1356.
[89] T.S. Basu Baul, D. Dutta, A. Duthie, N. Guchhait, B.G.M. Rocha, M.F.C.G. da Silva, R.B. Mokhamatam, N. Raviprakash, S.K. Manna, New dibutyltin(IV) ladders: Syntheses, structures and, optimization and evaluation of cytotoxic potential employing A375 (melanoma) and HCT116 (colon carcinoma) cell lines *in vitro*, J. Inorg. Biochem. 166 (2017) 34–48.
[90] M.E.K. Stathopoulou, N. Zoupanou, C.N. Banti, A.P. Douvalis, C. Papachristodoulou, K.D. Marousis, G.A. Spyroulias, T. Mavromoustakos, S. K. Hadjikakou, Organotin derivatives of cholic acid induce apoptosis into breast cancer cells and interfere with mitochondrion; Synthesis, characterization and biological evaluation, Steroids 167 (2021) 108798.
[91] W. Jiang, Q. Qin, X. Xiao, Y. Tan, Diorganotin(IV) complexes based on tridentate ONO ligands as potential anticancer agents, J. Inorg. Biochem. 232 (2022) 111808.
[92] E.C. Cheung, K.H. Vousden, The role of ROS in tumour development and progression, Nat. Rev. Cancer 22 (2022) 280–297.
[93] T.S. Basu Baul, M.R. Addepalli, A. Duthie, P. Singh, B. Koch, H. Gildenast, U. Englert, I. Rojas-León, H. Höpfl, Triorganotin(IV) derivatives with semirigid heteroditopic hydroxo-carboxylato ligands: synthesis, characterization, and cytotoxic properties, Appl. Organomet. Chem. 35 (2021) e6080.
[94] M. Whiteman, J.S. Armstrong, N.S. Cheung, J.-L. Siau, P. Rose, J.-T. Schantz, D. P. Jones, B. Halliwell, Peroxynitrite mediates calcium-dependent mitochondrial dysfunction and cell death via activation of calpains, FASEB J. 18 (2004) 1395–1397.